1-1-2018

Patient-Specific Quantification of the Relationship Between the Left Atrium Pressure and the Ostial Diameter of the Left Atrial Appendage

Sky Tianqi Gao
University of Denver

Patient-Specific Quantification of the Relationship Between the Left Atrium Pressure and the Ostial Diameter of the Left Atrial Appendage

Abstract

The left atrial appendage has been a historically understudied region of the heart until fairly recently with the new understanding of its role in the stroke pathway of patients with atrial fibrillation. The goal of this study is to take a look at the biomechanical behavior of the left atrium and left atrial appendage under normal physiological loading conditions using material properties taken from biaxial stretch tests. Several different options for material properties models were tested and biaxial stretch test data of cadaveric human tissue samples for the left atrium and appendage were fit to a Fung-type strain-energy function for input into simulation. Simulations were performed on geometry of the left atrium and appendage extracted from computed tomographical images of a single patient spanning from the pulmonary veins to the mitral valve annulus. Physiological pressure loading conditions were simulated at 5 mmHg, 7.5 mmHg, 10 mmHg, 15 mmHg, and 20 mmHg over two cardiac cycles. Results showed that peak stresses and strains were concentrated at branches in the atrium as well as the ostial entrance to the appendage. Ostial diameter of the appendage was measured across to axes and showed increases from a baseline of 1.347 cm x 2.927 cm in the unloaded configuration up to a size of 1.749 cm x 3.219 cm in the loaded configuration. Finite element simulations may be a useful tool for improving patient treatment options, especially when it comes to mechanical left atrial appendage occlusion devices.

Document Type

Thesis

Degree Name

M.S.

Department

Mechanical Engineering

First Advisor

Ali N. Azadani, Ph.D.

Keywords

LAA, Left atrial appendage, Appendage, FEA, Finite element analysis

Subject Categories

Biomechanics | Cardiology | Cardiovascular System | Physiology

Patient-Specific Quantification of the Relationship between the Left Atrium Pressure and the Ostial Diameter of the Left Atrial Appendage

---

A Thesis

Presented to

the Faculty of the Daniel Felix Ritchie School of

Engineering and Computer Science

University of Denver

In Partial Fulfillment

of the Requirements for the Degree

Master of Science

---

by

Sky Gao

November 2018

Advisor: Ali N. Azadani

Author: Sky Gao
Title: Patient-Specific Quantification of the Relationship between the Left Atrium Pressure and the Ostial Diameter of the Left Atrial Appendage
Advisor: Ali N. Azadani
Degree Date: November 2018

ABSTRACT

The left atrial appendage has been a historically understudied region of the heart until fairly recently with the new understanding of its role in the stroke pathway of patients with atrial fibrillation. The goal of this study is to take a look at the biomechanical behavior of the left atrium and left atrial appendage under normal physiological loading conditions using material properties taken from biaxial stretch tests. Several different options for material properties models were tested and biaxial stretch test data of cadaveric human tissue samples for the left atrium and appendage were fit to a Fung-type strain-energy function for input into simulation. Simulations were performed on geometry of the left atrium and appendage extracted from computed tomographical images of a single patient spanning from the pulmonary veins to the mitral valve annulus. Physiological pressure loading conditions were simulated at 5 mmHg, 7.5 mmHg, 10 mmHg, 15 mmHg, and 20 mmHg over two cardiac cycles. Results showed that peak stresses and strains were concentrated at branches in the atrium as well as the ostial entrance to the appendage. Ostial diameter of the appendage was measured across to axes and showed increases from a baseline of 1.347 cm x 2.927 cm in the unloaded configuration up to a size of 1.749 cm x 3.219 cm in the loaded configuration. Finite element simulations may be a useful tool for improving patient treatment options, especially when it comes to mechanical left atrial appendage occlusion devices.

TABLE OF CONTENTS

List of Figures

CHAPTER 1: INTRODUCTION

The left atrial appendage is a small bulbous extension of the left atrium that forms early in development from the venous pole of the heart[1]. In recent years, the importance of the left atrial appendage (LAA) and its role in the disease progression of patients, especially those with atrial fibrillation, has risen to the forefront of the field of interventional cardiology[2]. The dynamic behavior of the LAA throughout the cardiac cycle is not well understood from a biomechanical standpoint, and has been difficult to investigate using traditional medical imaging methods such as tomography or magnetic resonance imaging. The structure of the LAA makes it particularly susceptible to formation of blood clots, and this increased chance of thrombosis is one of the leading causes of morbidity in patients with atrial fibrillation, mitral valve disease, or other heart diseases.

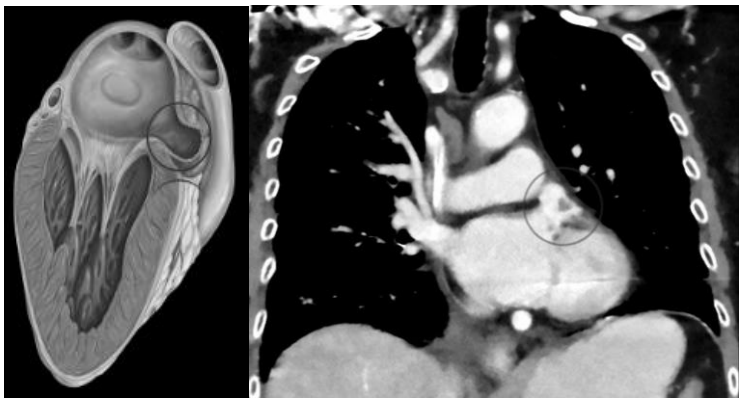

Fig 1.1: Left atrial appendage location in the heart. Cartoon and CT scan (coronal plane)
Patrick J. Lynch, medical illustrator - Wikimedia Commons

Current medical treatments range from clot management through drugs such as warfarin to the usage of mechanical closure devices. Mechanical LAA closure devices were originally approved in the United States by the FDA in 2015 with the WATCHMAN device, and usage has since increased in prevalence dramatically[3]. Data from the five-year follow-up on PREVAIL and PROTECT-AF clinical trials of the device shows that these mechanical occlusion devices have similar stroke reduction benefits as warfarin therapy. Of the 1,114 patients participating in the trial, patients using the mechanical occlusion device had a 55% reduction in fatal stroke, mainly hemorrhagic. These treatment options have been relatively successful with low rates of complication, but complications that do occur are often dangerous or fatal due to their placement in the heart. In the case of mechanical occlusion devices, a deeper understanding of the biomechanical behavior of the left atrial appendage with regards to both normal and diseased atrial pressures could provide a better framework for the design and usage of such devices. The present study seeks to expand the current understanding of the dynamics of the left atrial appendage and its relationship to left atrial pressure through both finite element modeling as well as experimental testing in order to better inform clinical decisions and improve patient health outcomes.

CHAPTER 2: BACKGROUND

2.1 Heart Background

The heart is located inside the rib cage, slightly to the left of the mid-sagittal plane, and contains four chambers. Atria are smaller, superior chambers that receive blood, while ventricles are noticeably larger, inferior chambers that pump blood to the body.

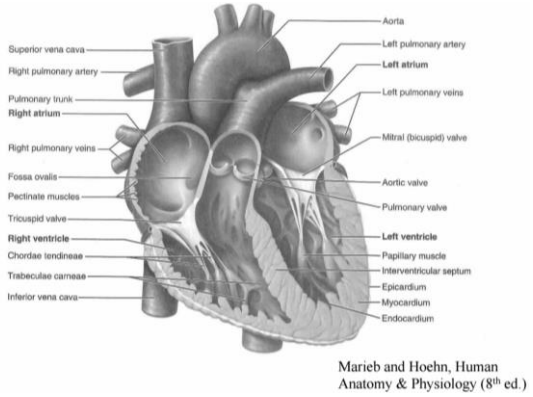

Fig 2.1: Gross anatomy of the normal human heart

Oxygenated blood leaves from the lungs and enters the left atrium, and is then pumped by the left ventricle throughout the body, before arriving at the right atrium. From there, it is pumped to the lungs by the right ventricle, and finally arrives at the left atrium, completing the cycle. Due to the different functions of the left and right sides of the heart, there are size and pressure differences between the two halves. Specifically, the left chambers of the heart are larger, and contain about three times as much muscle as the right chambers[1].

Naturally, these functional considerations result in different mechanical properties and geometries in the different regions of the heart.

The heart beats rhythmically and the beating is split into the systole and diastole phases, which are the contraction and relaxation phases of the tissue, respectively. The pressure and volume of the heart changes during each cycle, and many cardiac pathologies can be diagnosed by looking at abnormalities in pressure-volume plots of the heart chambers[10]. Typical stroke volumes (blood volume output per cycle) are in the range of 4L/min to 8L/min. Atrial pressure is typically in the 0mmHg to 20mmHg range, while ventricular pressure is typically in the 0mmHg to 120mmHg range, and these are important input parameters to understand when looking at treatment options for various heart pathologies.

2.2 Left Atrium and Cardiac Cycle

The left atrium is one of the four chambers of the heart previously mentioned, with the function of receiving oxygenated blood from the lungs and pumping the blood into the left ventricle for dispersal throughout the body (see Figure 1.1). To further elaborate, the left atrium serves as a preliminary pump that accounts for up to 30% of the filling of the left ventricle, and has a typical volume between 22mL to 58mL depending on the individual[9]. Throughout the normal cardiac cycle, atrial pressure is relatively stable, ranging between 0mmHg to 20mmHg in healthy individuals. Peaks in atrial pressure correspond with the atrial systole, which is the contraction of the atrium before ventricular systole, along with a slow build up of pressure during pre-filling of the chamber. Other

upticks in atrial pressure correspond with periods of isovolumetric contraction and isovolumetric relaxation, which is when the heart contracts or relaxes without volume change. These are due to the timed opening of the heart valves which requires pressure inside the corresponding chamber to reach a certain threshold pressure. In patients with cardiovascular disease, such as high blood pressure, atrial fibrillation, or valvular diseases, this healthy atrial pressure curve would be different to compensate for the effects of the various disorders.

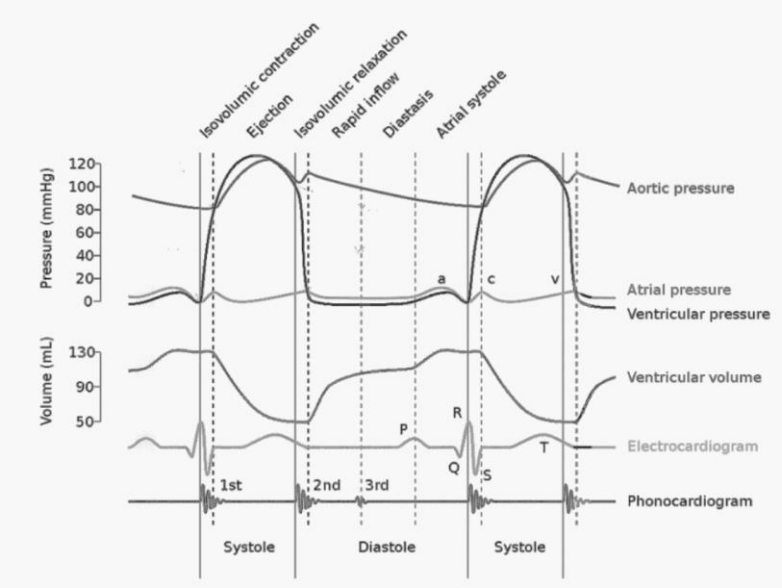

Fig 2.2: Two cycles of healthy cardiac cycle. Left atrial pressure varies from 0mmHg to 20mmHg with small peaks corresponding with isovolumetric contraction and relaxation as well as during atrial systole.
Wikimedia Commons revised work by DanielChangMD

The pressure curves of the normal cardiac cycle are important to understand because the pressure is the main force inside the heart and therefore the main contributor to changes in size of the various heart chambers. For this study, the primary focus will be upon the pressure inside the left atrium and how it affects the deformation of the LAA.

2.3 LAA Structure and Composition

The left atrial appendage is a small, tube-like structure connected to the main body of the left atrium but is composed of tissue with distinct structural, physiological, and material properties. With the advent of improved medical imaging, the importance of the LAA in certain pathological pathways has become better understood. The ostial entrance to the LAA is readily noticeable, and distinguished by a circumferential reduction in size at the connection with left atrium. When compared with the tissue comprising the left atrium, LAA tissue is slightly more distensible, which helps facilitate its function as a decompression chamber during periods of atypically high left atrial pressure[4]. The main body of the LAA develops as an outgrowth of the embryonic left atrium and forms into a smooth-walled bulbous space with a comb-like pattern of pectinate muscles inside. Typical morphological shapes have been described, classified, and designated as the "chicken wing", "cactus", "windsock", and "cauliflower" shapes, in order of prevalence[5]. The shape and size of the LAA varies dramatically between individuals, with volumes ranging from 0.7mL to 19.2mL[6]. Generally speaking, the LAA of patients with atrial fibrillation are both more voluminous as well as presenting with a larger ostial diameter. Size of the LAA additionally demonstrates sex-related variations along with changes with age[5].

Males have a larger LAA on average and the physical dimensions of the LAA generally increase with age with an approximate ostium size of 0.8-1.2 cm, width of 1.0-1.8 cm, and length of 2.1-2.9 cm when measured excised. The interior of the LAA is filled with pectinate muscle throughout, contributing significantly to its difference in mechanical properties when compared with the left atrium proper. The thickness of the pectinate

muscle varies with age and sex but is on the order of 1 mm and uniform throughout the LAA. In older individuals, the LAA tends to be larger overall. As previous studies have shown, the size, shape, and composition of each individuals LAA can vary drastically and this may play an important role in the success rates of various interventions targeting the region.

2.4 LAA Physiology

The main function of the LAA appears to be as an important regulator in heart rate, left atrial volume, and preload volume[5]. The LAA has several properties that make it suited for this purpose. When compared to the left atrium, it is superior in position, meaning that it will only fill properly during periods of higher pressure. Additionally, the LAA is more distensible from a material properties standpoint when compared with the myocardium comprising the left atrium. The cardiac cycle also has a markedly different presentation in the LAA when compared to the left atrium. The main difference is that the LAA has its own distinct pattern of contraction. Blood flow in the appendage in patients with healthy sinus rhythm tend towards a biphasic pattern of blood flow, but a large portion of the population experiences an extra filling and contraction movement in each flow cycle. The first emptying action occurs shortly after diastole and is followed by a period of backflow while the second set of flows occurs at the same time as atrial systole. The first inflow-outflow pattern is thought to be caused by squeezing of the LAA against the pericardium as it is pushed underneath by the enlarging ventricle while the second inflow-outflow

pattern is due to blood flow in the atrium. The LAA itself also shows some electrical activity and active contraction corresponding with the noted pattern of blood flow.

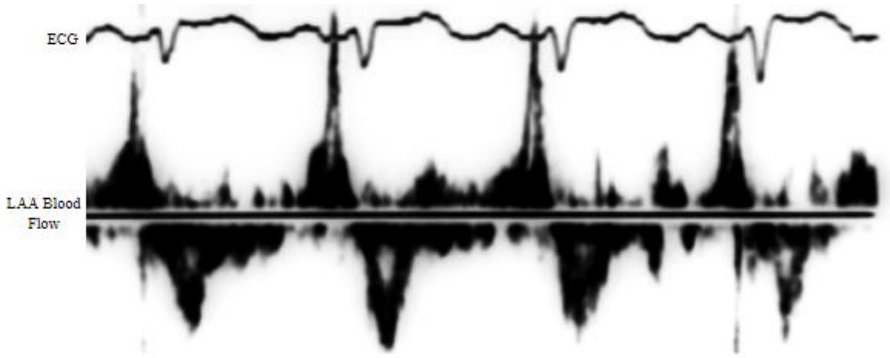

Fig 2.3: Four phase blood flow pattern in the LAA with ECG comparison. Spikes in the signal above the straight line indicate flow exiting the LAA while spikes below indicate inflow into the LAA. The spikes in blood flow correspond with atrial systole and atrial diastole. Wikimedia Commons

Historically, the importance of the LAA in heart pathologies was overlooked but with recent discoveries of its importance in pathophysiologies, notably atrial fibrillation, developing a deeper understanding of its biomechanical behavior has become more important.

2.5 LAA Pathology

The LAA plays a key role in the pathological pathway of thromboembolism, especially in patients with atrial fibrillation (AF). In this pathway, the LAA serves as an initiation site for the formation of the thrombus, which may then dislodge and eventually result in ischemic stroke[7]. With AF being one of the most prevalent cardiac arrhythmias, the importance of understanding the mechanical behavior of the LAA cannot be understated. Atrial fibrillation is a disease characterized by a rapid and irregular cardiac cycle and studies have shown that in patients with atrial fibrillation and recent embolic

event, up to 41% may present with thrombus in the left atrial appendage[8]. The most commonly seen pathological change of the heart accompanying AF is increased fibrosis of the atria due to any number of factors such as genetics, age, valvular heart disease, hypertension, or congestive heart failure. These changes contribute and clash with the normal electrical signal conduction system which causes the disorganized, erratic heartbeat that patients with AF experience. The exact pathophysiological pathway leading from atrial fibrillation to thrombus formation in the left atrial appendage has not yet been fully described, but prevailing theories implicate the complex blood flow cycle previously described in the LAA. This complex cycle would be impacted significantly by an unhealthy sinus rhythm, such as that present in AF patients, which may lead to the incomplete expulsion of blood from the grooved interior of the LAA, leading to eventual thrombus formation. As the major complication of AF does come from the increased risk of thrombus formation in the LAA, many treatments target the LAA region in order to diminish clotting. Luckily, thromboembolism in the LAA is the only major pathology involving the LAA. Nonetheless, a better understanding of the stresses and strains that the LAA goes through during the cardiac cycle should allow for improvements to be made in current treatments, and may help in discovering new treatment methods.

2.6 Treatment Options

For patients with AF, the current standard of care calls for treatment with blood thinners such as warfarin. While these treatments have been effective for reducing the risk of thrombosis and ischemic stroke by preventing blood clotting, patients with other complications may be contraindicated for treatment with blood thinners. For these patients, mechanical closure with LAA closure devices has seen success. Typically the device is inserted with a catheter, using transesophageal ultrasound as guidance. After the device is maneuvered into the ostial entrance of the LAA, the device can be expanded to fit snugly in the opening. The woven mesh fabric-like material promotes tissue formation, which will eventually seal off the region, preventing flow of blood into and out of the LAA. In the United States, the WATCHMAN device is currently the only FDA approved percutaneous LAA occlusion device but Europeans also have access to the Amplatzer plug device, which functions similarly. Data from the latest WATCHMAN clinical trial follow-up indicates that the mechanical closure device has a lower primary event rate when compared with standard warfarin treatment in the following categories: overall stroke rate, ischemic stroke, hemorrhagic stroke, and cardiovascular or unexplained death[11].

Mechanical occlusion devices are generally made of a shape retaining nickel-titanium alloy, commonly referred to as nitinol. This nitinol mesh is then surrounded by a permeable polyester fabric, which will facilitate clotting and the eventual sealing off of the appendage. They are typically guided into the correct location through a combination of fluoroscopy and transesophageal echo, which are both standard, non-invasive methods for visualizing the heart region. Once guided to the correct location, the device is then allowed

to expand to its original shape, and hooks, along with the shape of the nitinol wireframe allows it to stay lodged inside the ostial opening of the LAA. The WATCHMAN device in particular comes in 5 different sizes, with ostial diameter starting at 21 mm and increasing in increments of 3 mm. Common sizing procedure includes increasing blood volume with fluids and then measuring the largest ostial diameter opening[36].

Table 2-1. WATCHMAN Device Sizing

LAA Diameter (mm)	*Device Diameter (mm)*	*Device Compression (mm)*
17-19	21	16.8-19.3
20-22	24	19.2-22.1
23-25	27	21.6-24.8
26-28	30	24.0-27.6
29-31	33	26.4-30.4

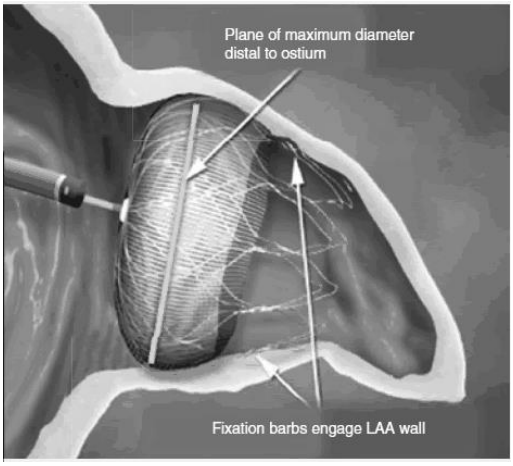

Fig 2.4: WATCHMAN left atrial appendage occlusion device made of a nitinol wireframe and polyester mesh. The device is guided into place using imaging in conjunction with a catheter and lodges in place at the point of maximum ostial diameter.

2.7 Finite Element Analysis

Finite element modelling is a useful analytical tool that will be used heavily in this work. Finite element modelling sees widespread use throughout many industries, mainly as an investigative tool that can take imaging data and build a computational framework for testing scenarios that are difficult or impossible to test in the traditional experimental sense. Specifically, this study will look at the deformation of the LAA throughout the cardiac cycle, something which has many clinical applications, but is difficult and expensive to test *in vivo*. The resulting ostium size of the LAA, which is the size of the opening leading to the LAA, is of particular clinical significance because current treatment options target this region and seek to occlude blood flow to the LAA to prevent the formation of a thrombus. Other important factors that will be considered are the stresses and strains that the LAA experiences throughout both normal as well as abnormal cardiac cycles.

The finite element method is an analysis technique to find approximate solutions to partial differential equations by subdividing the domain into many small elements. In each interval, proper functions are chosen so that the overall solution represents the full partial differential equation. These functions are generally piecewise defined polynomial functions that are solved over each element using methods from linear algebra. It is an iterative process that works to minimize an associated error function until certain convergence criteria are reached. Simple finite element models can be solved by hand, but more complex 3-D models, such as is used in this study, rely on clever programming algorithms and numerical approximations to reduce the computation time.

CHAPTER 3: MATERIAL PROPERTIES

Due to the relatively obscure location and size of the LAA as well as its downplayed role in cardiac health, research into the accurate measurements of the LAA is a fairly new field of study. The vast variation seen between individuals makes study of the material properties of the LAA a difficult task, but improvements in imaging technology may also lead to improvements in this area. Experimentally, LAA material properties have been investigated in a multitude of animal models, but data from human tissue is fairly rare. Another complication is the living nature of the tissue, as material properties performed on animals or on cadaveric tissue cannot fully account for the electro-mechanical properties present in living tissue. Because there is a significant difference in tissue mechanical properties between animal models[20] and human tissue[19], both are necessary for a thorough understanding of the LAA. Animal models contribute greatly to the general trends in tissue property and provide much easier accessibility, while data from human tissues is limited and often restricted to individuals of old age. Here we provide a brief overview of the models commonly used in the field of cardiac biomechanics.

3.1 Cardiac Tissue Structure

In order to develop an understanding of the mechanics involved with the LAA, an understanding of the physiology and microstructure of cardiac tissue must first be mentioned. Cardiac tissue is composed primarily of myocardium, which is a form of muscle tissue. This cardiac muscle is a highly organized tissue composed of repeating units called sarcomeres. These sarcomeres are organized from bundles individual strands of cells known as myofibrils, which utilize the proteins actin and myosin to contract. In addition to the cardiac muscle, connective tissue such as collagen and other interstitial molecules also contribute to around 30% of the heart tissue, by mass[35].

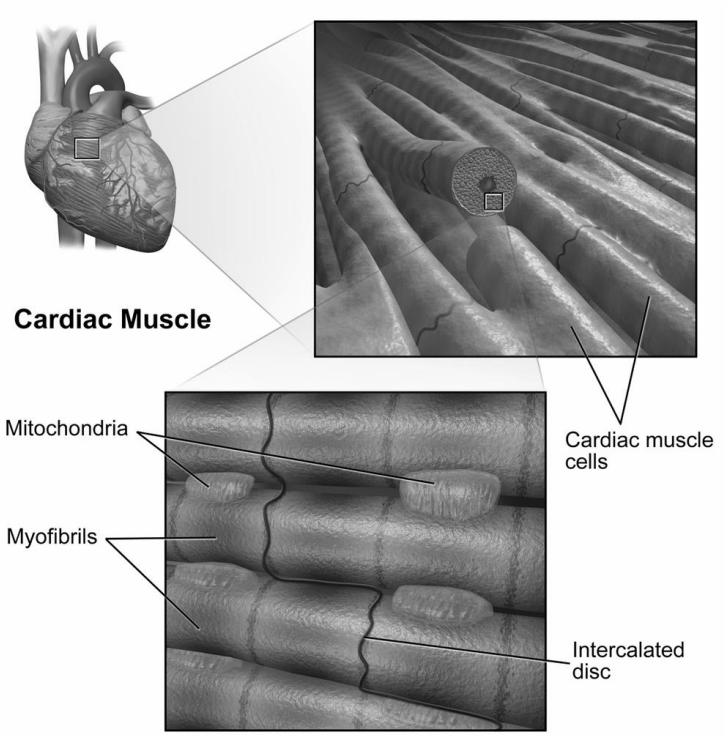

Fig 3.1: Microstructure of cardiac muscle. Myofibrils form into bundled units called sarcomeres which provide the contraction of the muscle. Intercalated discs between adjacent units allows for steady signal conduction and a healthy sinus rhythm.
OpenStax College - Anatomy & Physiology Wikimedia Commons

Cardiac muscle tissue is the primary tissue present in the heart, and forms the bulk of the tissue in the heart wall. While similar to skeletal muscle, there are some key differences between the two types of muscle tissue. The primary difference is that cardiac muscle is more interconnected when compared with skeletal muscle. Cardiac muscle cells are deeply interconnected through junctions known as intercalated discs, which allows for its smooth, patterned contraction. Another difference is that cardiac muscle contains its own calcium ion source which is necessary for healthy heart contraction.

Orientation of the fibers making up the cardiac muscle varies throughout the thickness of the tissue. This can be seen clearly in Figure 3.2, which outlines the variations in cardiac muscle orientation throughout the thickness of the left ventricle.

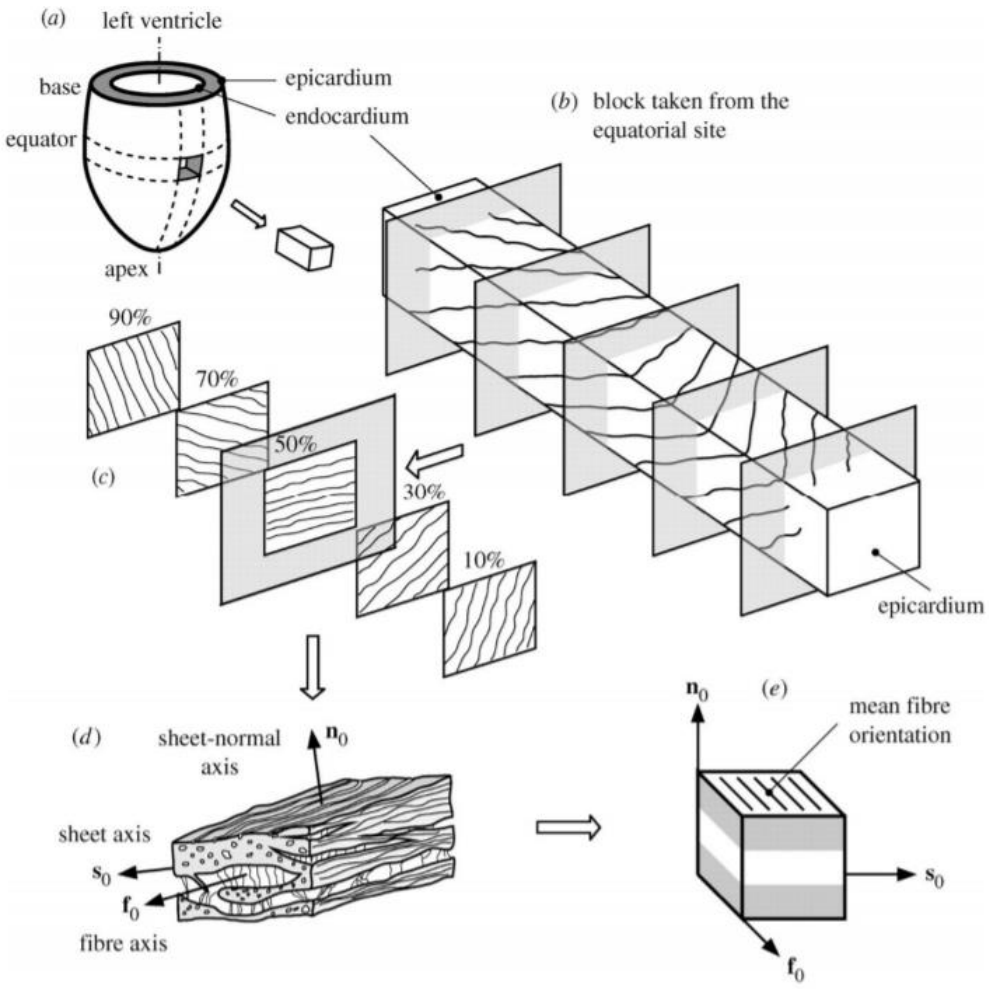

Fig 3.2: (a) Left ventricle and cutout; (b) shows the variation in fibre orientation throughout the block of tissue through the thickness of the cardiac muscle; (c) varying degrees of fibre orientation; (d) natural material coordinate system label defined through the fibre orientation; (e) local material coordinate system defined through mean fibre orientation[18]

For the purposes of mechanical analysis, it is natural to define a 3-dimensional coordinate system corresponding with the fiber orientation present in cardiac muscle. These material axes correspond with: in-line with fiber orientation, transverse to the fiber orientation, and the normal perpendicular to the fiber orientation plane, as seen in Figure 3.2 (e). This understanding forms the basis for most of the models currently used in heart research.

3.2 Review of Material Models

In this chapter, the most prevalent material models of passive myocardium is described. While material models that include the effects of electrical conduction do exist, the difficulty in collecting experimental data on live tissue has made it difficult to assign accurate parameters necessary for those models. Passive myocardium models also face this relative lack of experimental data, but accurate material models can be generated from a constitutive basis, and this type of model is the most commonly used. Due to the microstructure of cardiac muscle, it can be described as an orthotropic material. To further complicate things, passive cardiac tissue also has time-dependent properties including stress-relaxation and slight hysteresis.

In the literature, a number of constitutive models with varying degrees of complexity have been investigated and these will be described briefly[12]. These can generally be categorized as either transversely isotropic models or orthotropic models. The basis for both types of models are rooted in fundamental equations of continuum mechanics. Cardiac tissue, as with most soft tissue, can be assumed to be incompressible which gives us

$$J = \det \mathbf{F} \equiv 1$$

where **F** is the deformation gradient, using the standard conventions of continuum mechanics. We define the right and left Cauchy-Green tensors

$$\mathbf{C} = \mathbf{F}^{\mathbf{T}}\mathbf{F} \text{ and } \mathbf{B} = \mathbf{F}\mathbf{F}^{\mathbf{T}} \tag{1}$$

and the Green strain tensor

$$\mathbf{E} = \frac{1}{2}(\mathbf{C}\text{-}\mathbf{I}), \tag{2}$$

where **I** is the identity tensor. The principle isotropic invariants of the Cauchy-Green tensor is then

$$I_1 = \text{tr } \mathbf{C}, \quad I_2 = \frac{1}{2}[I_1^2 - \text{tr}(\mathbf{C}^2)], \quad \text{and} \quad I_3 = \det \mathbf{C}. \tag{3}$$

For models which consider anisotropy, further invariants can be defined as

$$I_4 = \mathbf{a}_0 \cdot (\mathbf{C}\mathbf{a}_0), \quad I_5 = \mathbf{a}_0 \cdot (\mathbf{C}^2\mathbf{a}_0), \quad I_6 = \mathbf{b}_0 \cdot (\mathbf{C}\mathbf{b}_0), \quad I_7 = \mathbf{b}_0 \cdot (\mathbf{C}^2\mathbf{b}_0) \tag{4}$$

where $\mathbf{a}_0$ and $\mathbf{b}_0$ are the unit vectors in the prefered reference directions of the anisotropic equations. The relationship between $\mathbf{a}_0$ and $\mathbf{b}_0$ is denoted by the coupling invariant

$$I_8 = \mathbf{a}_0 \cdot (\mathbf{C}\mathbf{b}_0) = \mathbf{b}_0 \cdot (\mathbf{C}\mathbf{a}_0). \tag{5}$$

With these invariants, we can then describe the cardiac tissue as a hyperelastic material through the use of a strain energy density function, and the models that have been used successfully in the literature are predominantly these types of models.

An example of a transversely isotropic model based on a constitutive consideration of fiber orientation was the Humphrey et al. model with the form

$$\Psi = c_1(\sqrt{I_4} - 1)^2 + c_2(\sqrt{I_4} - 1)^3 + c_3(I_1 - 3) + c_4(I_1 - 3)(\sqrt{I_4} - 1) + c_5(I_1 - 3)^2 \tag{6}$$

with invariants I_1 and I_4.

The classical orthotropic material model for soft tissue is the Fung-type model[40], with form

$$\mathrm{W} = \frac{c}{2}(e^Q - 1) + \frac{1}{D}\left(\frac{J_{el}^2 - 1}{2} - \ln J_{el}\right) \tag{7}$$

with W denoted as strain-energy, *c* and *D* as material constants, and J_{el} as the elastic volume ratio. With the assumption of incompressibility, which is valid for most soft tissue, Equation 7 simplifies to

$$\mathrm{W} = \frac{c}{2}(e^{Q} - 1) \tag{7}$$

where

$$Q = b_{ijkl} E_{ij} E_{kl}. \tag{8}$$

Q can be written explicitly as

$$Q = b_{1111}E_{11}^2 + b_{2222}E_{22}^2 + 2b_{1122}E_{11}E_{22} + b_{1212}E_{12}^2 + 2b_{1112}E_{12}E_{11} + 2b_{2212}E_{12}E_{22} \tag{9}$$

which reduces to

$$Q = b_{11}E_{11}^2 + b_{22}E_{22}^2 + 2b_{12}E_{11}E_{22} \tag{10}$$

under assumptions of negligible shear terms, such as might be found in biaxial testing. Equations 9 and 10 are drastically simplified with the previously mentioned assumptions, to get an idea of the full scope of the model, the number of components of *b* would be 21 for a fully anisotropic model and 9 for an orthotropic model.

$$\mathbb{b}_{\text{anisotropic}} = \begin{bmatrix} b_{1111} & b_{1122} & b_{1133} & b_{1123} & b_{1113} & b_{1112} \\ & b_{2222} & b_{2233} & b_{2223} & b_{2213} & b_{2212} \\ & & b_{3333} & b_{3323} & b_{3313} & b_{3312} \\ & & & b_{2323} & b_{1323} & b_{1223} \\ & \text{Symmetic} & & & b_{1313} & b_{1213} \\ & & & & & b_{1212} \end{bmatrix}, \mathbb{b}_{\text{orthotropic}} = \begin{bmatrix} b_{1111} & b_{1122} & b_{1133} & 0 & 0 & 0 \\ & b_{2222} & b_{2233} & 0 & 0 & 0 \\ & & b_{3333} & 0 & 0 & 0 \\ & & & b_{2323} & 0 & 0 \\ & \text{Symmetic} & & & b_{1313} & 0 \\ & & & & & b_{1212} \end{bmatrix} \tag{11}$$

Most orthotropic models for myocardium are of the Fung exponential type, with increasing complexity and number of parameters. In these models, the parameters, generally denoted with *c*-subscripts, are fit with experimental data from bi-axial testing in

order to then use the models to predict material behavior. The primary material model used in this study is a generalized Fung-type hyperelastic model of the form described in the equation above.

CHAPTER 4: METHODS AND MATERIALS

4.1 Experimental Data Collection

For the purposes of developing a deeper understanding of the mechanical behavior of the left atrium and its appendage, several bi-axial tests and digital image correlation tests were performed on fresh sheep hearts to verify material properties data from previous experiments that were available for final input into the finite element model. All specimens used for experimental data collection were procured from an abattoir with good practices. Sheep hearts were collected after slaughter through the throat cut/heart stick protocol and maintained in a refrigerated space until data collection, and all data was collected within 96 hours.

Bi-axial testing was performed with a BioTester planar stretching system (CellScale, ON). Tissue samples excised from the left atrial appendage and left atrium of sheep were cut into a square shape taking care to keep fiber orientation either parallel or normal to the edges. Specimens were mounted onto the bi-axial testing machine using a set of CellScale biorakes, which were used to secure each of the four edges. The specimens were gently set into a saline bath maintained at 37 degrees Celsius. The upper surface of the specimens was carefully seeded with a random pattern of graphite in order to provide contrast for the built in camera system, which operated at 15Hz. Prior to stress-strain measurements, each sample was preconditioned through 10 cycles of 10% equi-biaxial

strain. Stress data was extracted from the load cells connected to each arm of the BioRake system, while strain data was extracted from the deformation tracking system in the CellScale LabJoy camera system. In total, 9 samples from the left atrial appendage were tested and 6 samples from the left atrium were tested and these results were compared with previous in-lab data to verify the material properties for use in the finite element model.

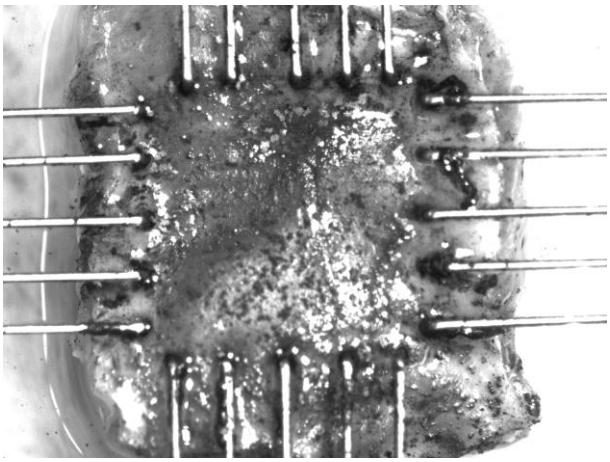

Fig 4.2: Representative set-up for bi-axial stretch testing of a sample of ovine left atrium. BioRakes supply orthogonal stretching and strain is monitored through an overhead camera that tracks the graphite flakes scattered on the surface of the sample.

4.2 Finite Element Modelling

For the patient-specific finite element model, left atrium geometry was reconstructed from available computed tomographic angiography (CTA) data. From this data, an accurate three-dimensional representation of the left atrium, left atrial appendage, mitral valve annulus, and the pulmonary veins could be generated. The raw CTA image data was collated through the image processing software ScanIP (Synopsis, CA) and imported into the Rapidform (3D Systems, SC) software for smoothing before finally being meshed in HyperMesh (Altair, MI) to generate the mesh necessary for the finite element

model. At this time, a simple pressure loading configuration was also used to perform a convergence study in order to determine the density of the mesh. The model was discretized into a mesh of triangular shell elements and thickness was found using an iterative process based on conservation of mass. After meshing the model, the four pulmonary veins and the mitral valve annulus were fixed in space in the ABAQUS software package, material properties were applied, and several different loads were applied in order to explore the behavior of the left atrium and appendage under physiological loading conditions.

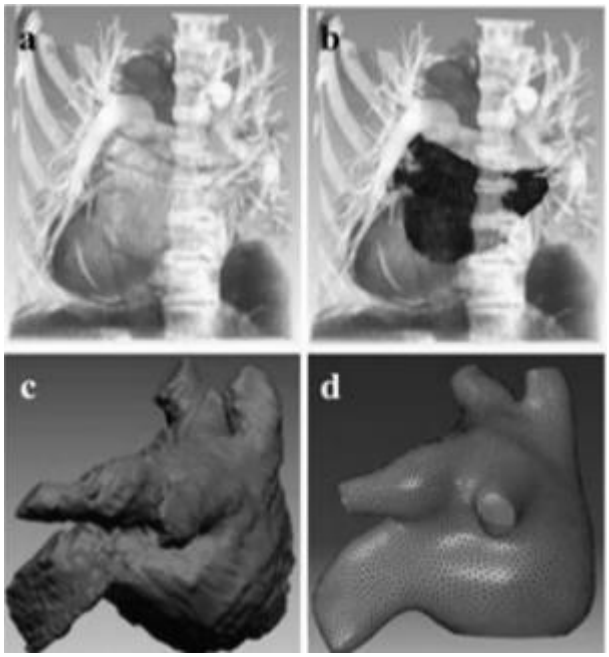

Fig 4.5: Construction of the 3D patient-specific geometry
a) CTA scans, b) Image slices used for reconstruction, c) Extracted geometry, d) smoothed and meshed model for computational simulation.

Simulations were conducted at pressures maximums of 0 mmHg, 5 mmHg, 10 mmHg, 15 mmHg, 20 mmHg through a simple linear loading curve to test model integrity. Simulations were then also conducted at the same pressure maximums based on a physiological loading curve from two cycles of normal left atrial pressure during the

cardiac cycle, and these simulation data were used for the final results. Two final simulations at 7.5 mmHg were also conducted, once with the normal physiological left atrial pressure curve and once using a modified pressure curve representing the pressures that would be present in the cardiac cycle of a patient with atrial fibrillation. From the simulation results, maximum in-plane stresses and measurements of the ostial opening length were extracted and compared.

CHAPTER 5: RESULTS

5.1 Experimental Material Properties – Animal

A representative stress-strain curve from a biaxial test of ovine left atrial appendage is shown below. Full stress-strain data can be found in the appendix.

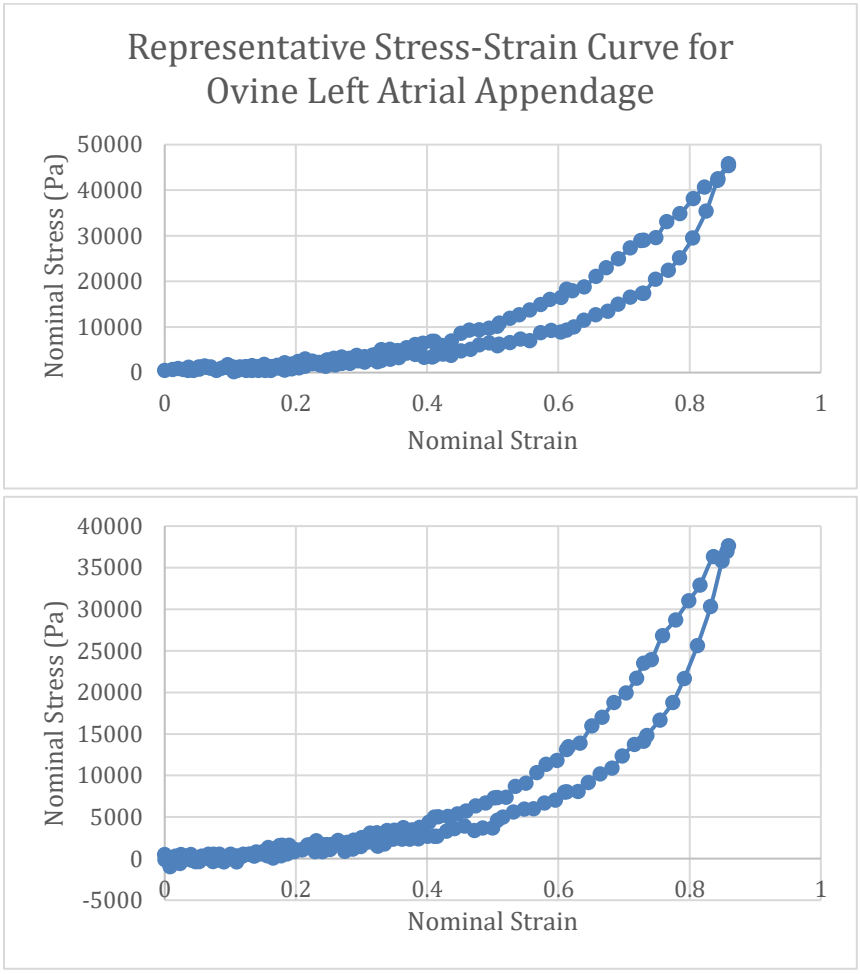

Fig 5.1.1: Nominal stress-strain curve for ovine tissue sample
Top: Cross-fiber, Bottom: In-fiber

5.2 Experimental Material Properties – Human

Stress-strain data from the left atrium and left atrial appendage of human heart tissue was fit to a 4-parameter Fung-type hyperelastic model using raw bi-axial stretch data provided by previous data from Bellini et al[19]. The form of the strain-energy function used was

$$W = \frac{C}{2}(e^{Q} - 1), \quad Q = c_{11}E_{11}^2 + 2c_{12}E_{11}E_{22} + c_{22}E_{22}^2 \quad . \tag{11}$$

A Levenberg-Marquardt least squares algorithm in MATLAB was used to fit the parameters and yielded the following material coefficients for the left atrium and left atrial appendage.

Table 5-1. Parameters for Fung material model of left atrium and left atrial appendage from human tissue under biaxial stretch

	b_{11}	b_{12}	b_{22}	C
Left Atrium	19.4398	8.9172	12.6544	1.2425
LAA	11.4896	12.9766	12.2372	0.9737

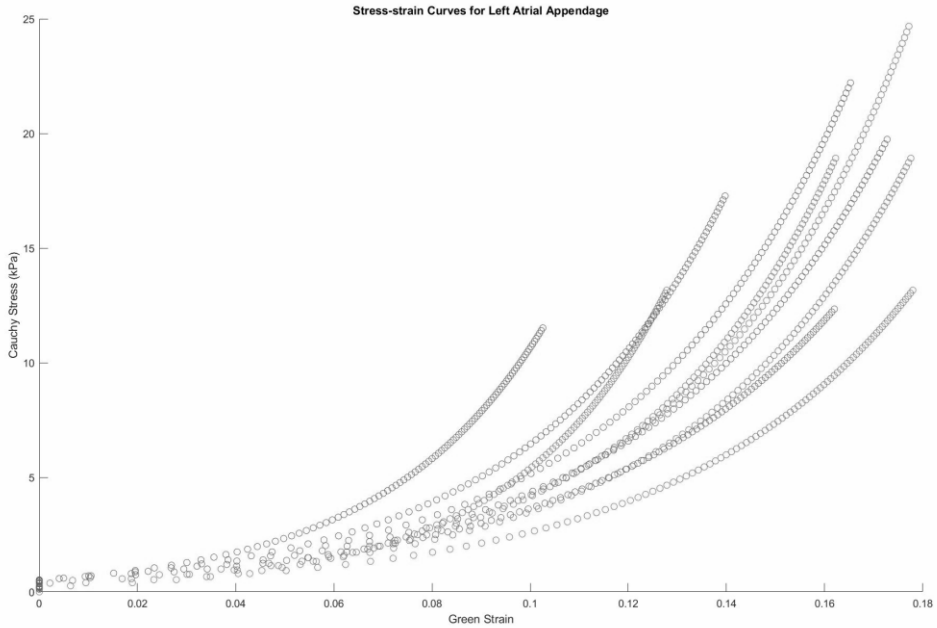

Figure 5.2.1: Cauchy Stress vs. Green Strain for excised samples of human left atrial appendage as tested by biaxial stretch. (n=10)

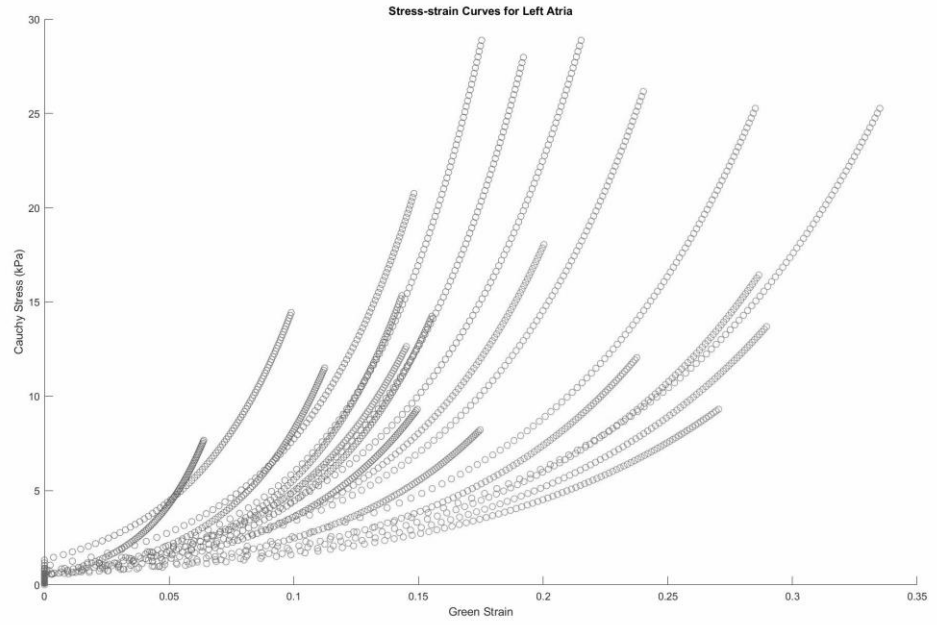

Figure 5.2.2: Cauchy Stress vs. Green Strain for excised samples of human left atria as tested by biaxial stretch. (n=20)

The stress-strain data from the 10 left atrial appendage samples and 20 left atrium samples were then averaged and served as a tabular input for the Fung-type material model used in the ABAQUS patient-specific finite element model. To perform the data averaging, the Cauchy stresses at set intervals of strain were averaged into a single point for that strain region. This type of curve averaging is more appropriate to account for the non-linearity of soft tissue[37].

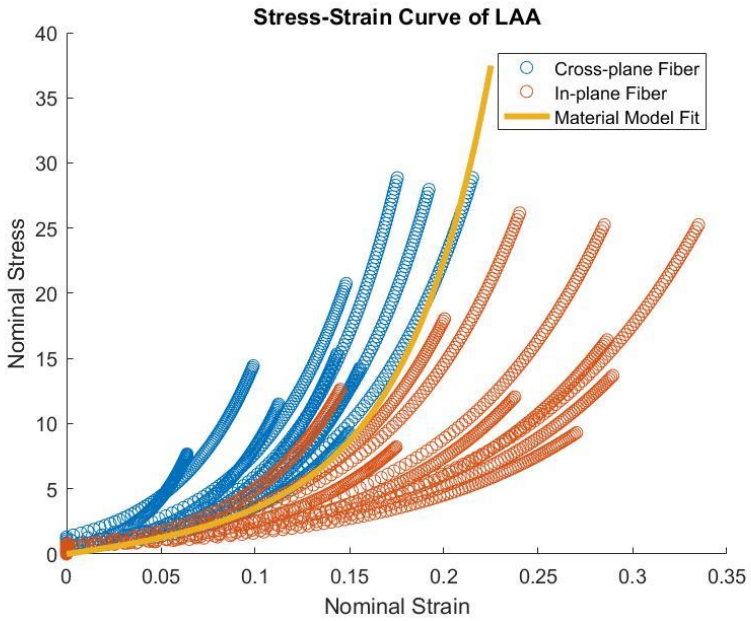

Fig 5.2.3 Stress-Strain Curve of LAA with Average Curve found through curve averaging, Nominal Stress (kPa) vs. Nominal Strain

Tissue anisotropy index[39] was calculated by finding the material constants for the cross-plane and in-plane fibers in the equi-biaxial state according to

$$\sigma_{11}^{equi} = (2E+1)E(c_{11}+c_{12})Cexp\{(c_{11}+c_{22}+2c_{12})E^2) \quad (12)$$

$$\sigma_{22}^{equi} = (2E+1)E(c_{12}+c_{22})Cexp\{(c_{11}+c_{22}+2c_{12})E^2) \quad (13)$$

and

$$K = \frac{2|c_{11}-c_{22}|}{(c_{11}+c_{22}+2c_{12})} \quad . \quad (14)$$

The resulting anistropy index of 0.27 for the left atrium and 0.06 for the left atrial appendage of these samples was both reasonably low so the a four-parameter Fung-type fit was used to generate stress-strain data for tabular input into ABAQUS biaxial table data. Boundary condition was chosen with the entrances to the pulmonary veins and the mitral valve annulus fixed because these regions of the anatomy have relatively little movement in the human body and are also far from the atrial appendage. In total, there were 15,535 nodes and 30,820 elements in the model. This very fine mesh ensures that the results converge. Stress-strain data from the appendage was used for the model because it was slightly more distensible than the left atrium. Tabulated data of the material properties used can be found in the Appendix, a hyperelastic material input with Poisson ratio of 0.499 was used.

5.3 Finite Element Simulations

The unloaded geometry of the finite element model of the left atrium and appendage was found to be 1.71mm using the backwards iterative method described in detail previously, which used the same method to find the unloaded reference geometry of a finite element model of abdominal aortic aneurysm[16]. The material properties that were used in the simulations were taken from bi-axial testing of human left atrium. To summarize briefly, an initial guess of 3mm thickness for the shell elements in the model were used. A negative hydrostatic pressure was then applied to the model and the resulting deformed model was re-pressurized with consideration of conservation of mass over an iterative optimization process until a node-by-node difference of less than 5% between the repressurized model and original model and the result of 1.71mm shell element thickness was used for the remaining simulations of the study. The loading curve used is shown in the figure below.

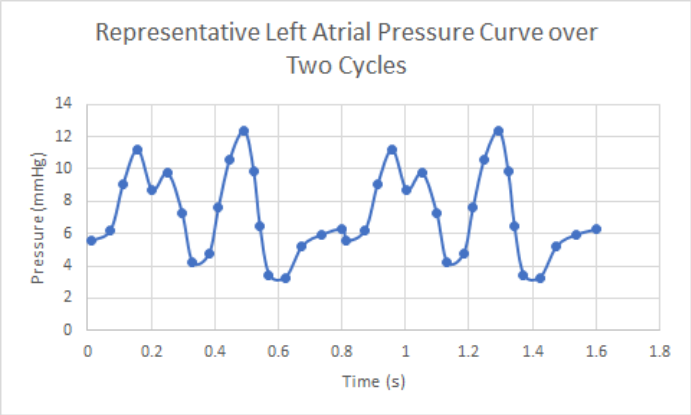

Fig 5.3: Representative left atrial pressure curve taken from data of healthy patients. Average pressure over 2 cycles is 7.25 mmHg with a minimum at 3.26 mmHg and a maximum at 13.39 mmHg. Heart rate 75 is bpm.

The undeformed 3-D model of the left atrium, generated as described, is shown in the figure below. At the top are the pulmonary veins which feed into the main body of the left atrium. At the left we see the left atrial appendage jutting out with ostial diameter encircled.

Fig 5.4: Undeformed geometry of the patient-specific finite element model. The encircled region is the ostial entrance to the left atrial appendage.

Nodal coordinates at the entrance of the left atrial appendage were selected manually and exported to MATLAB where the size of the opening was quantified. Distance between each node was calculated and due to the elliptical shape of the ostial opening, a long-axis and short-axis length are reported. Material properties were input according to the average stress-strain curve from biaxial stretching of human atrial tissue converted into nominal stress and nominal strain for the ABAQUS software package.

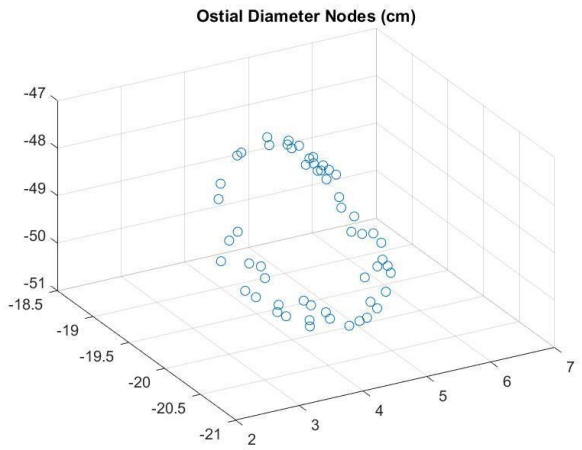

Fig 5.5: Extracted nodal locations of the ostial diameter for undeformed geometry of the model

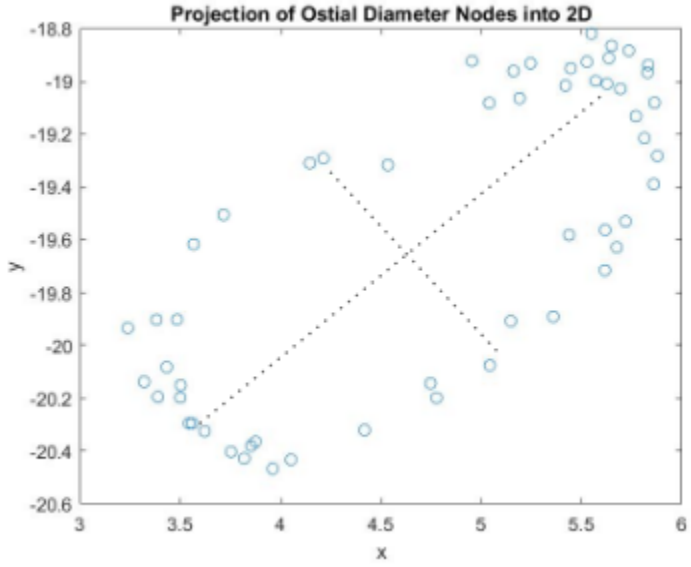

Fig 5.6: Projection of extracted ostial diameter nodes from the undeformed geometry. Long axis 2.927cm, short axis 1.347cm.

For the undeformed geometry of the patient-specific model, the ostial opening had a baseline size with long axis 2.93cm and short axis 1.35cm.

5 mmHg:

The normal left atrial pressure curve was then scaled linearly to an average of 5 mmHg compared to its original 7.25 mmHg and this loading curve was applied as an internal pressure surface force in ABAQUS.

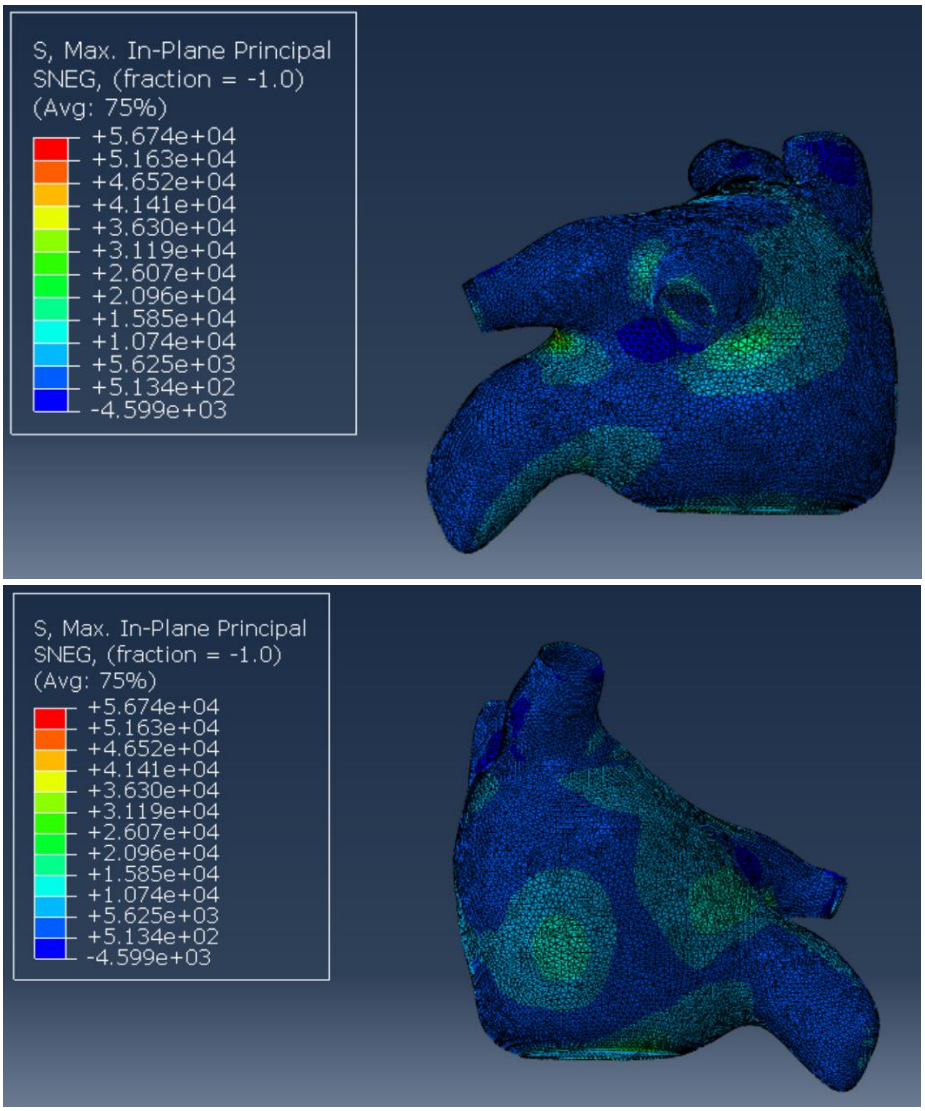

Fig 5.7.1: Maximum in plane principal stress with loading condition of 5 mmHg
Images taken from Peak Pressure of Second Cardiac Cycle
Top: Anterior view, Bottom: Posterior view

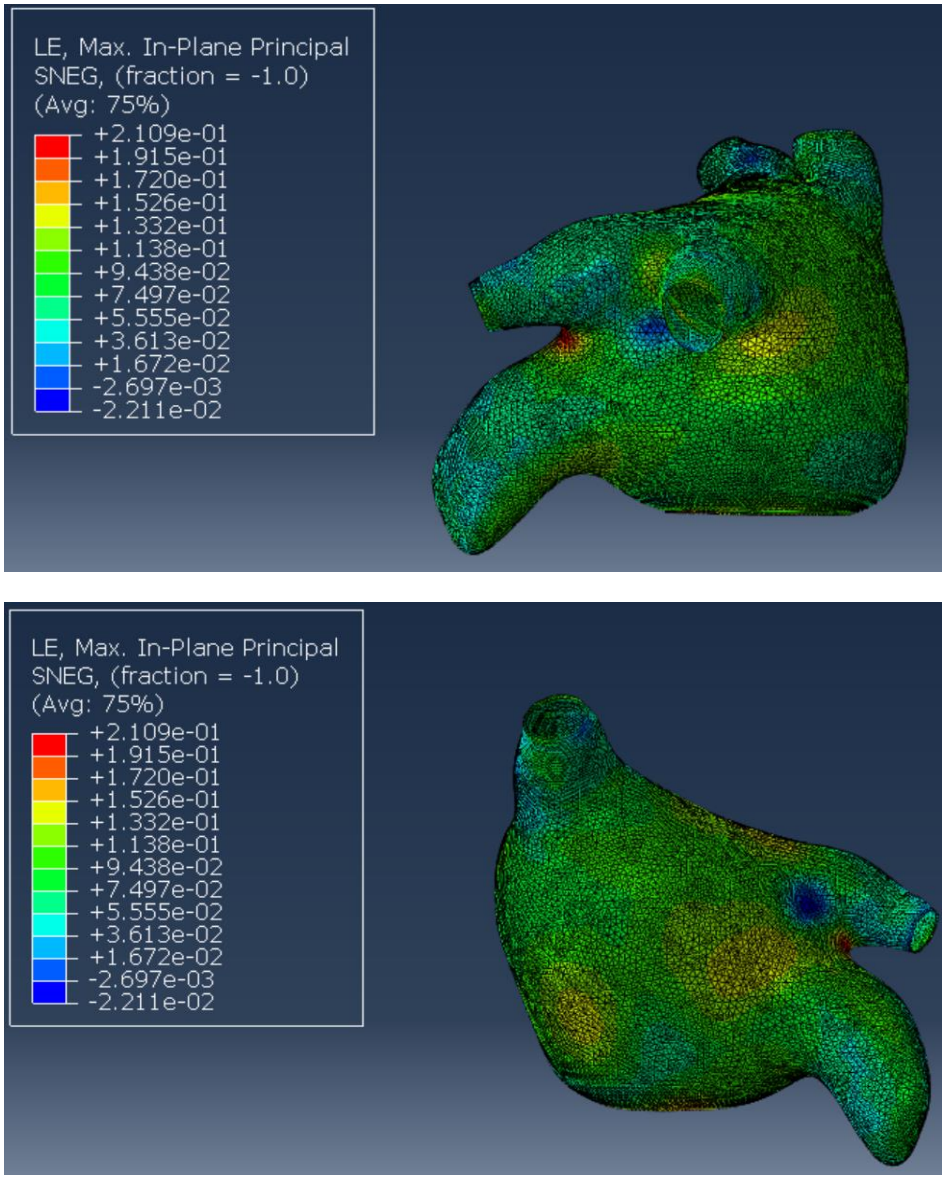

Fig 5.7.2: Maximum in plane principal strain with loading condition 5 mmHg
Images taken from Peak Pressure of Second Cardiac Cycle
Top: Anterior view, Bottom: posterior View

Maximum in plane principal stress for this loading condition peaked at 5.674×10^4 Pa. The simulation results show that peak stresses occur at locations where tissue branches off from the left atrium. Stresses in the appendage opening are also more focused on the short axis. Regions of higher strain were also limited to branching of the geometry, and had a maximum of 2.109×10^{-1}.

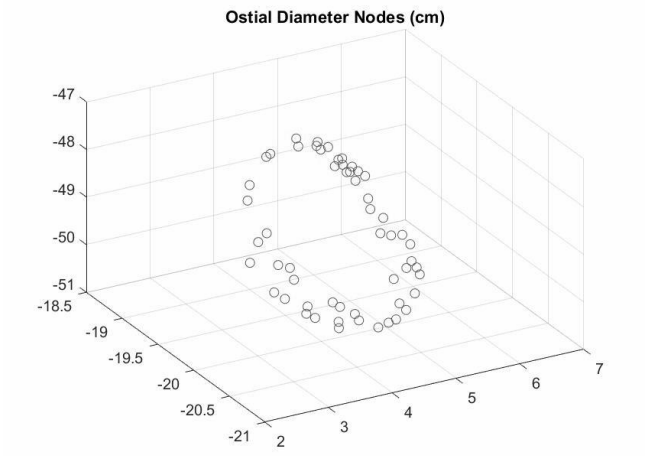

Fig 5.8: Extracted nodal locations of the ostial diameter for 5 mmHg loading condition

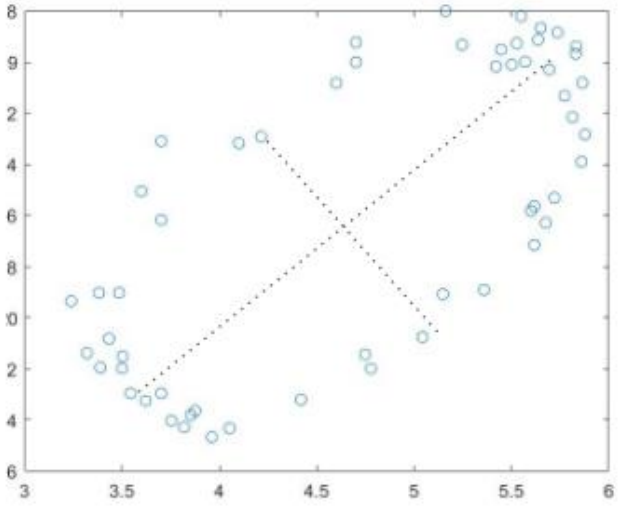

Fig 5.9: Projection of extracted ostial diameter nodes from 5 mmHg loading condition. Long axis 3.021cm, short axis 1.578cm.

Figures 5.8 and 5.9 show the nodal coordinates of the ostial opening to the left atrial appendage in 3-D and its projection, respectively. Separating the length of the ostial opening into a long and short axis yielded 3.021cm for the long axis and 1.578cm for the short axis.

10 mmHg:

Once again scaling the physiological left atrial pressure curve, an average pressure of 10 mmHg was used as the loading pressure on the internal surface of the geometry.

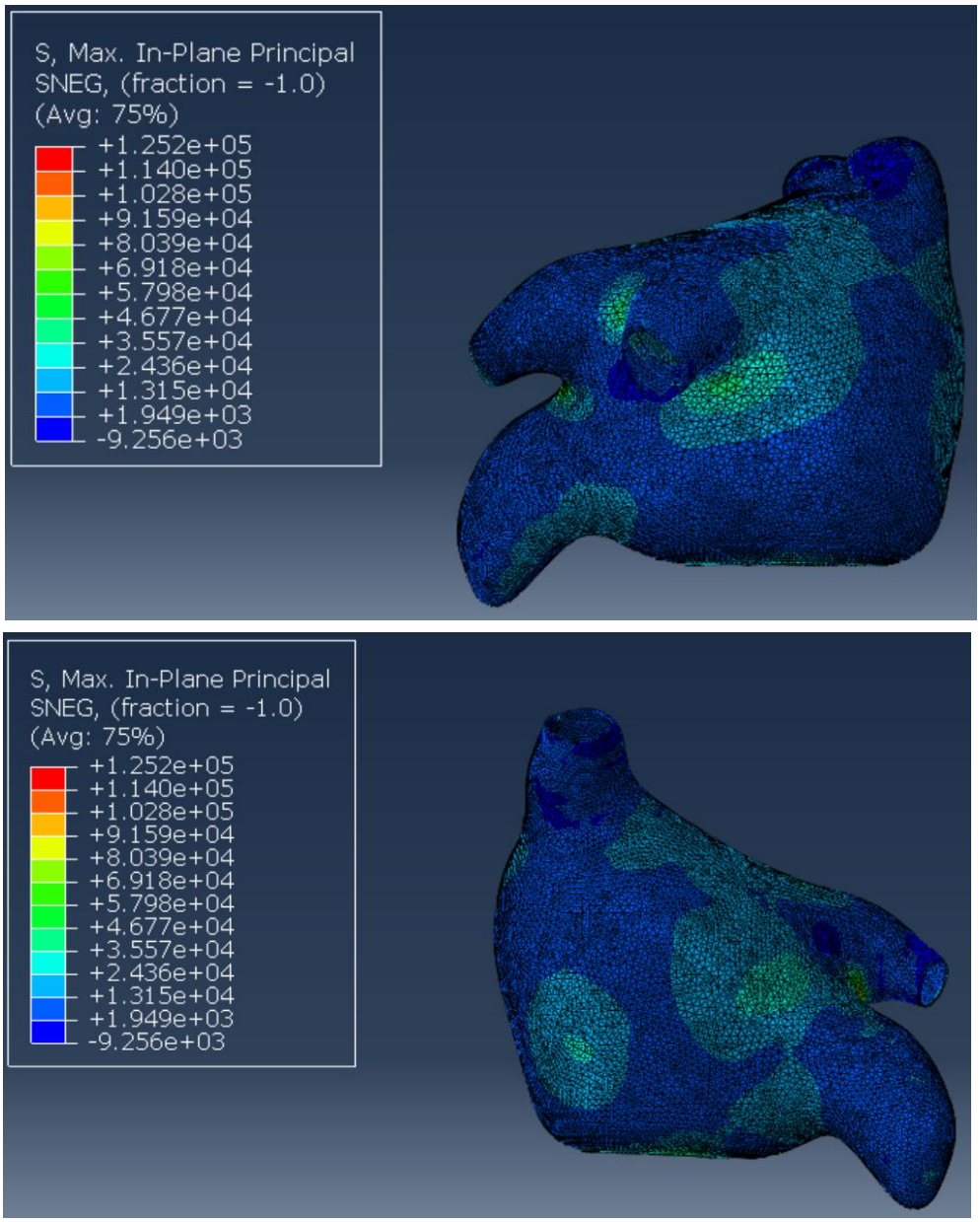

Fig 5.10.1: Maximum in plane principal stress with loading condition of 10 mmHg
Images taken from Peak Pressure of Second Cardiac Cycle
Top: Anterior view, Bottom: Posterior view

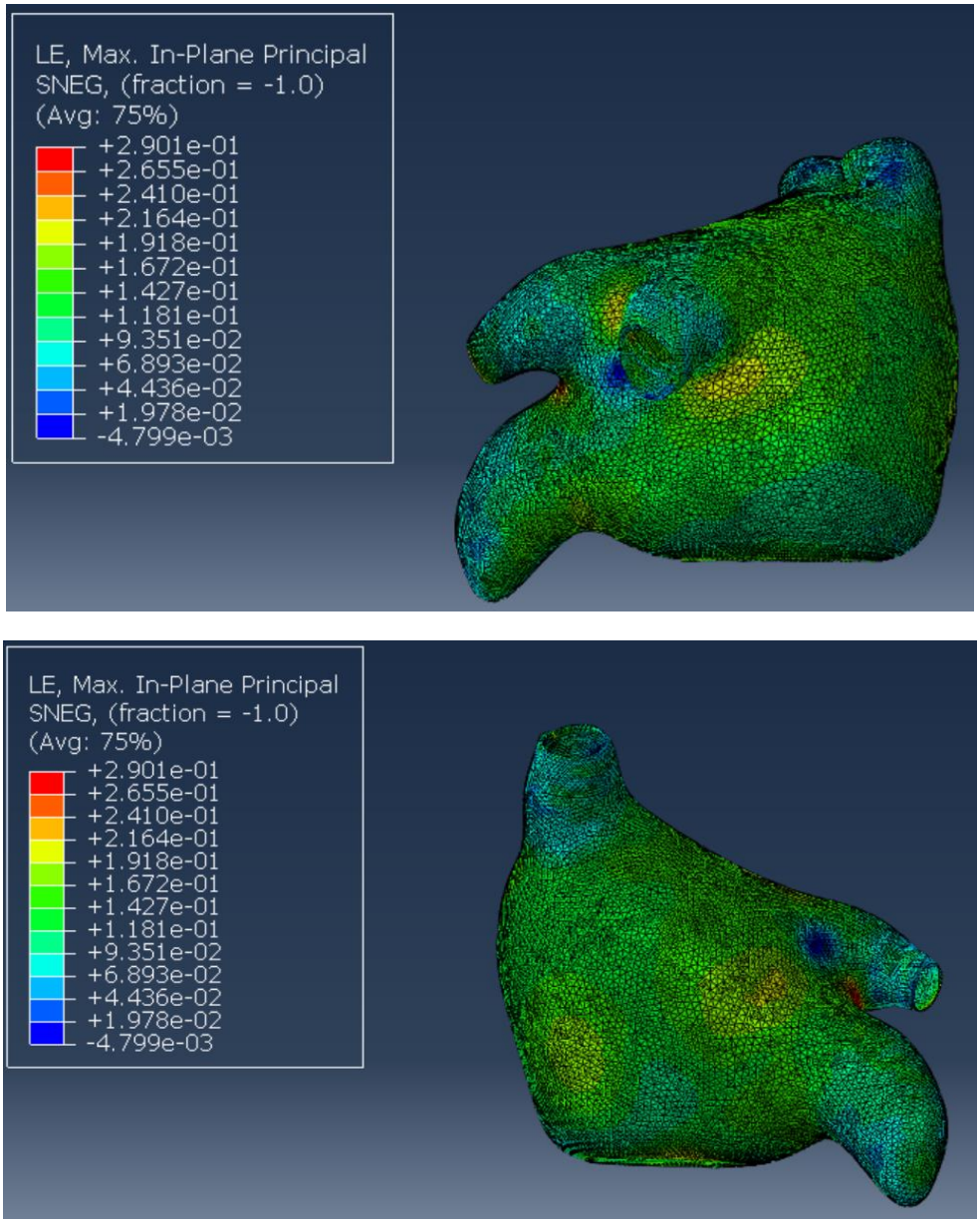

Fig 5.10.2: Maximum in plane principal strain with loading condition 10 mmHg
Images taken from Peak Pressure of Second Cardiac Cycle
Top: Anterior view, Bottom: posterior View

Maximum in plane principal stress for this loading condition peaked at $1.252x10^5$ Pa. Regions of higher stress remain the same compared to the 5 mmHg simulation, but are larger in magnitude and affect a larger portion of the left atrium body.

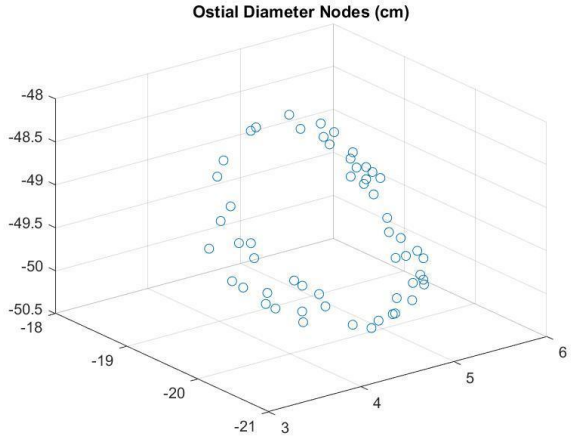

Fig 5.11: Extracted nodal locations of the ostial diameter for 10 mmHg loading condition

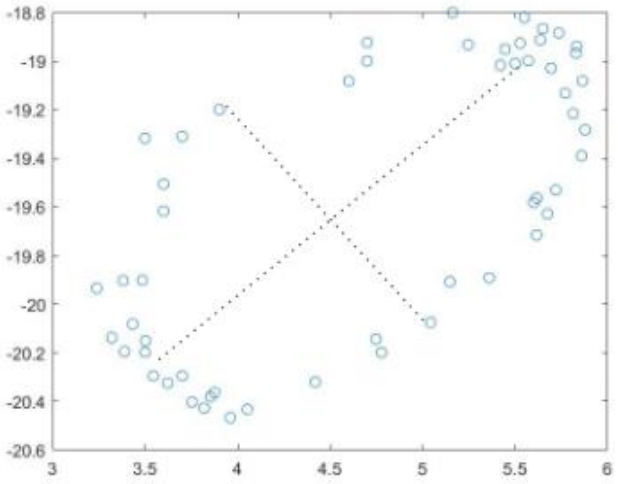

Fig 5.12: Projection of extracted ostial diameter nodes from 10 mmHg loading condition. Long axis 3.090cm, short axis 1.653cm.

Figures 5.11 and 5.12 show the nodal coordinates of the ostial opening to the left atrial appendage in 3-D and its projection, respectively. Separating the length of the ostial opening into a long and short axis yielded 3.090cm for the long axis and 1.653cm for the short axis.

15 mmHg:

Scaling the two-cycle left atrial pressure curve to an average of 15 mmHg and applying it as an internal surface load yielded simulation results show below.

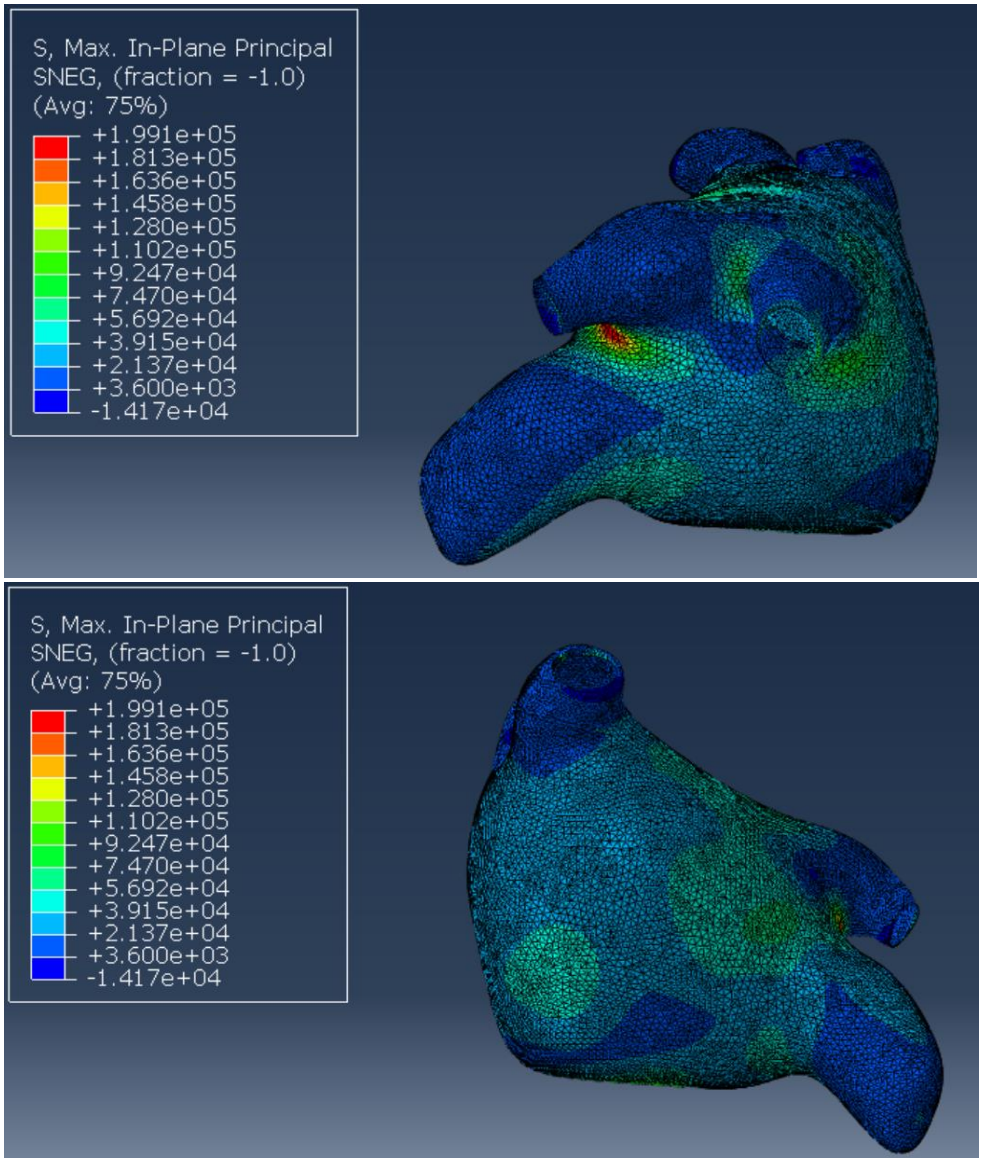

Fig 5.13.1: Maximum in plane principal stress with loading condition of 15 mmHg
Images taken from Peak Pressure of Second Cardiac Cycle
Top: Anterior view, Bottom: Posterior view

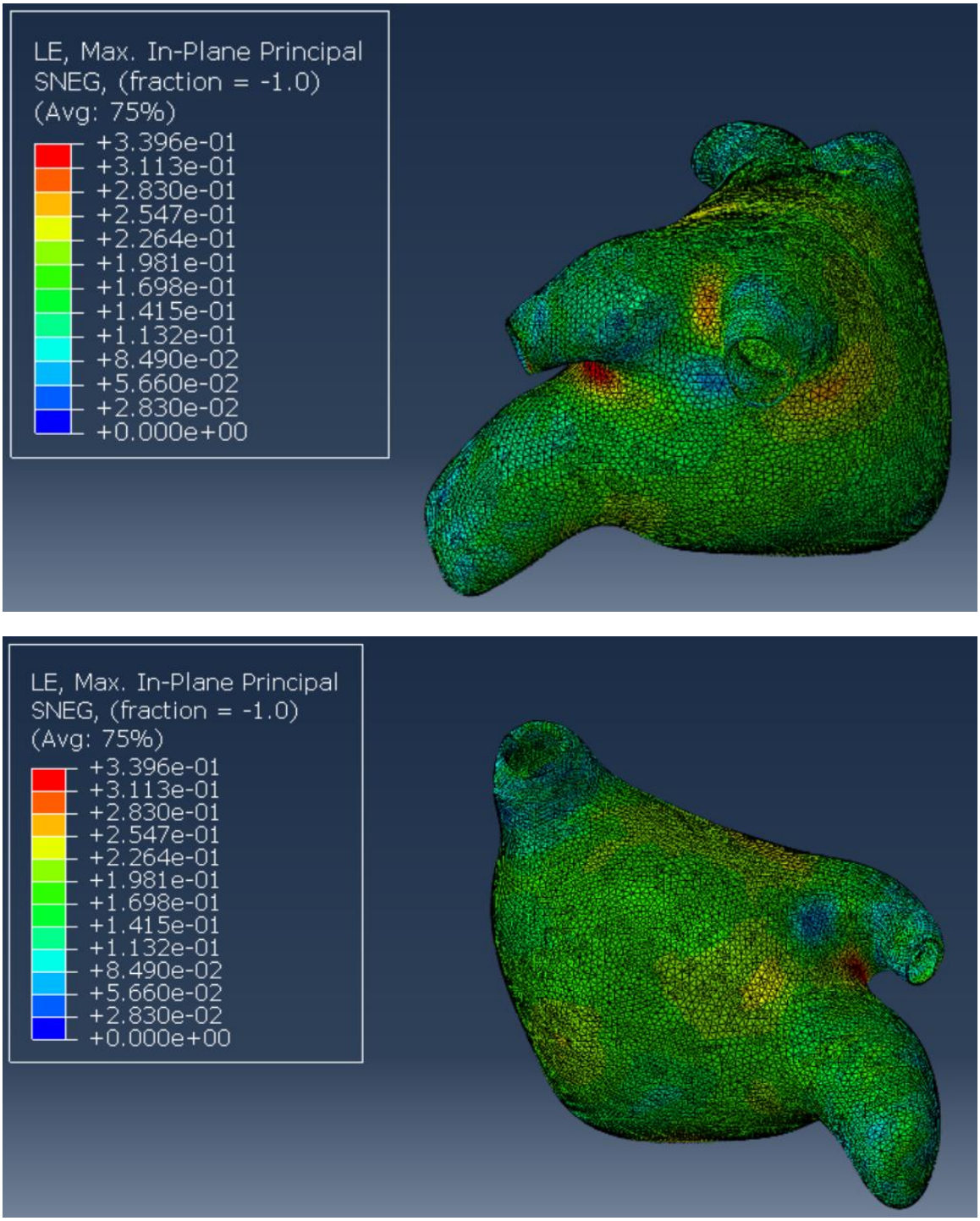

5.13.2:Maximum in plane principal strain with loading condition 15 mmHg
Images taken from Peak Pressure of Second Cardiac Cycle
Top: Anterior view, Bottom: posterior View

Maximum in plane principal stress for this loading condition peaked at $1.991x10^5$ Pa. Compared with the previous cases, there is significantly noticeably more in-plane principal stress throughout the entire body of the left atrium. The body of the appendage itself was relatively unstressed, but the ostial opening is the region of highest stress in the entire model.

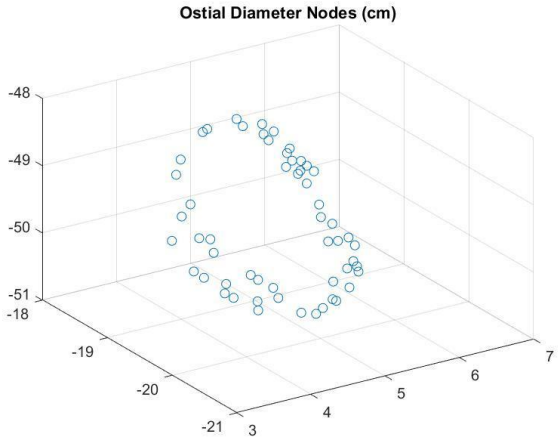

Fig 5.14: Extracted nodal locations of the ostial diameter for 15 mmHg loading condition

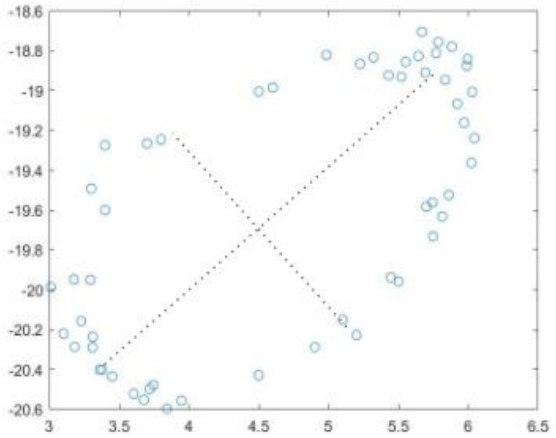

Fig 5.15: Projection of extracted ostial diameter nodes from 15 mmHg loading condition. Long axis 3.162cm, short axis 1.670 cm.

Figures 5.14 and 5.15 show the nodal coordinates of the ostial opening to the left atrial appendage in 3-D and its projection, respectively. Separating the length of the ostial opening into a long and short axis yielded 3.162cm for the long axis and 1.670cm for the short axis.

20 mmHg:

Using the same scaling technique, a left atrial pressure curve with average pressure 20 mmHg was generated and used as the loading curve in ABAQUS. Tables with all pressure loading curves used can be found in the Appendix.

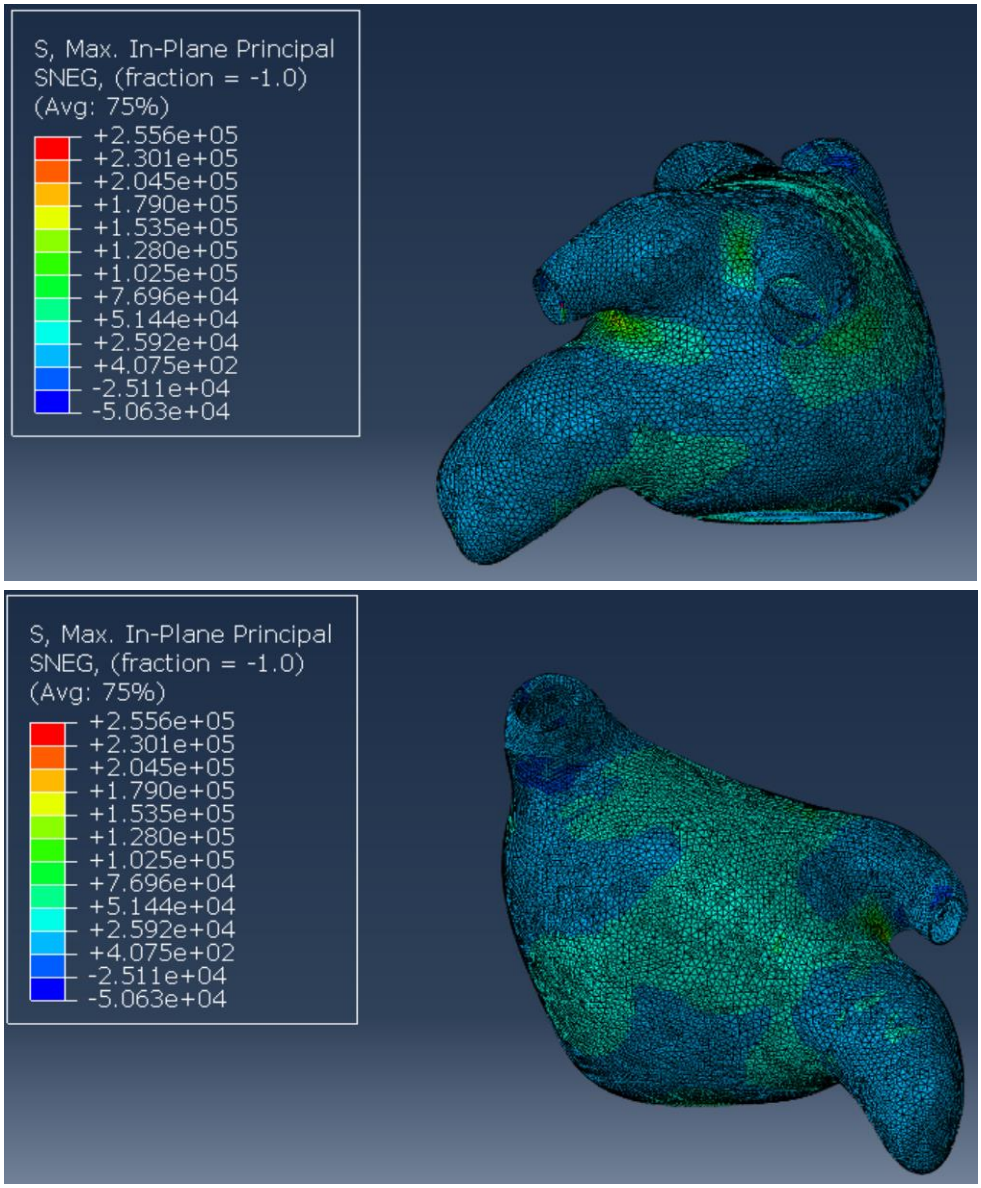

Fig 5.16.1: Maximum in plane principal stress with loading condition of 20 mmHg
Images taken from Peak Pressure of Second Cardiac Cycle
Top: Anterior view, Bottom: posterior View

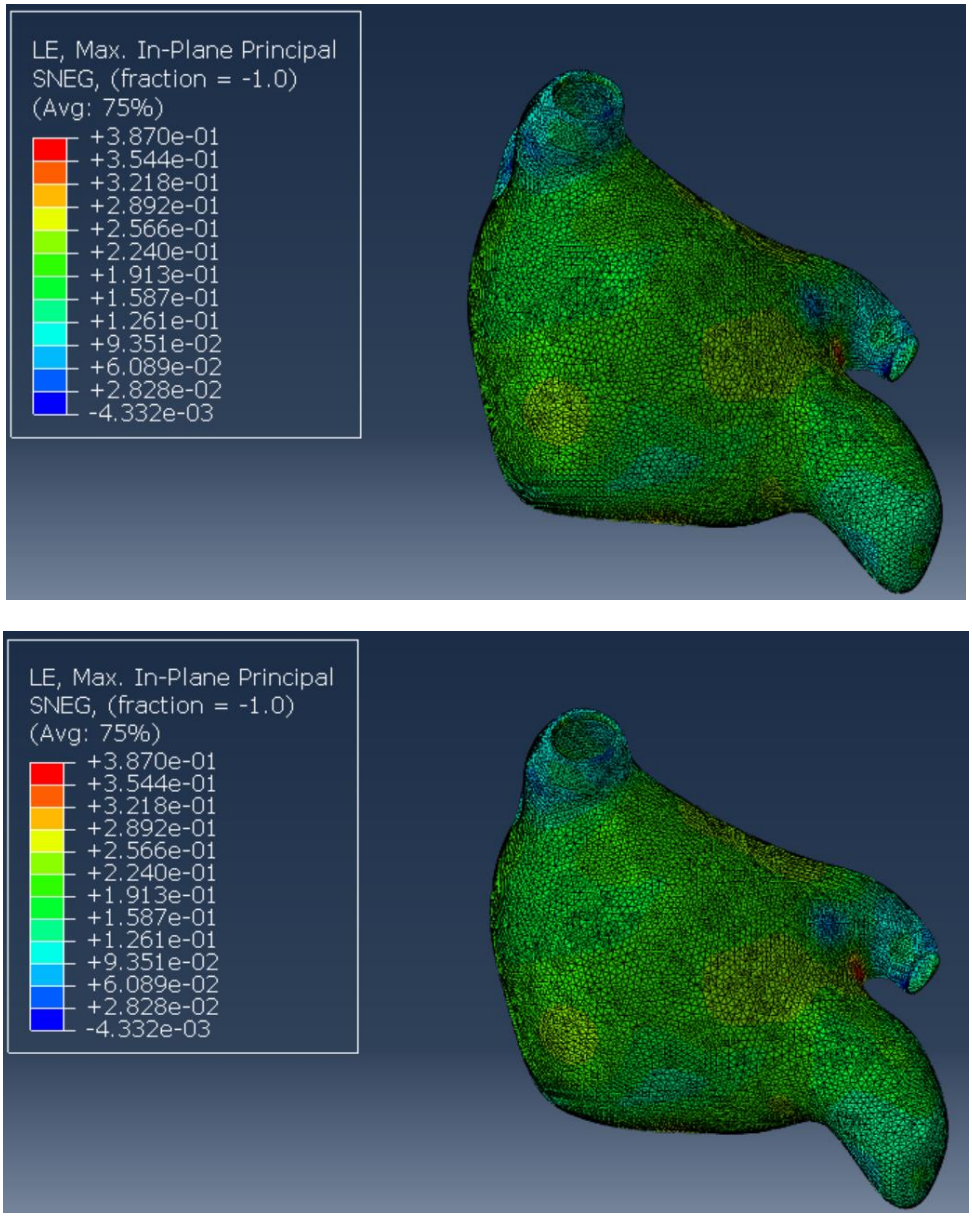

Fig 5.16.2: Maximum in plane principal strain with loading condition 20 mmHg
Images taken from Peak Pressure of Second Cardiac Cycle
Top: Anterior view, Bottom: posterior View

Maximum in plane principal stress for this loading condition peaked at $2.556x10^5$ Pa. Compared with the previous cases, there is significantly noticeably more in-plane principal stress throughout the entire body of the left atrium. The body of the appendage itself was relatively unstressed, but the ostial opening is the region of highest stress in the entire model.

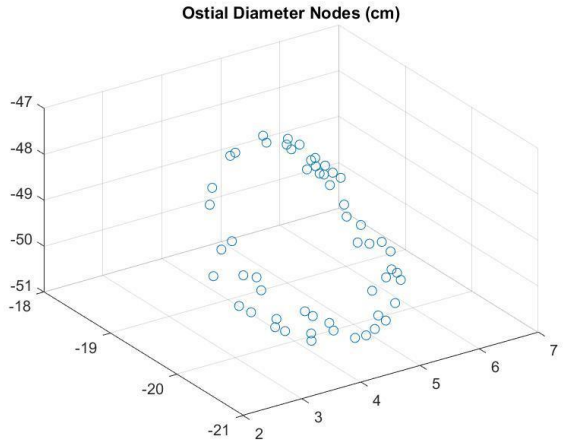

Fig 5.17: Extracted nodal locations of the ostial diameter for 20 mmHg loading condition

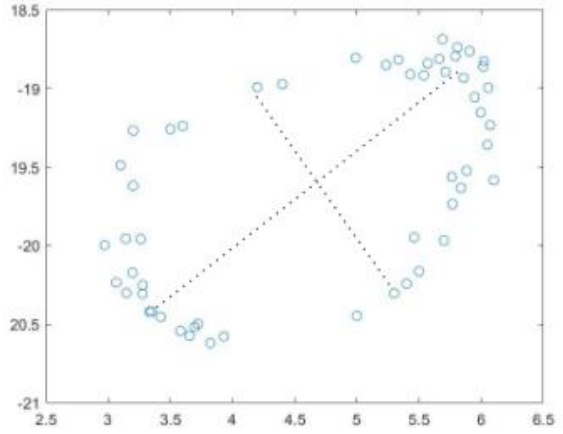

Fig 5.18: Projection of extracted ostial diameter nodes from 20 mmHg loading condition. Long axis 3.219cm, short axis 1.749 cm.

Figures 5.17 and 5.18 show the nodal coordinates of the ostial opening to the left atrial appendage in 3-D and its projection, respectively. Separating the length of the ostial opening into a long and short axis yielded 3.021cm for the long axis and 1.578cm for the short axis.

7.5 mmHg:

For the 7.5 mmHg loading condition, two cases were tested. One loading curve used was analogous to the previously discussed loading conditions, but modifications were made to the second loading curve to represent the left atrial pressures one might expect to see in a patient with atrial fibrillation. Specifically, the pressure peaks corresponding to the p-waves of the cardiac cycle were lowered and heart rate was increased to 100 bpm or 1.7 Hz compared to the original 75 bpm or 1.25 Hz. This test was done for comparative purposes, to see whether or not the left atrium of patients with atrial fibrillation would behave different mechanically do to the slight variation in loading condition pattern.

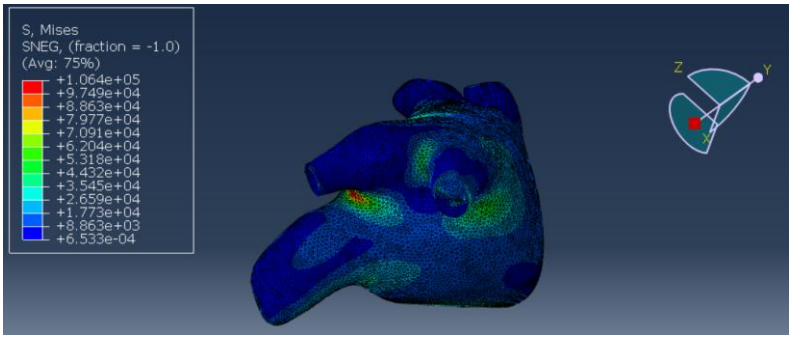

Fig 5.19: von Mises stress with healthy left atrial pressure loading condition of 7.5 mmHg Image taken from Peak Pressure of Second Cardiac Cycle

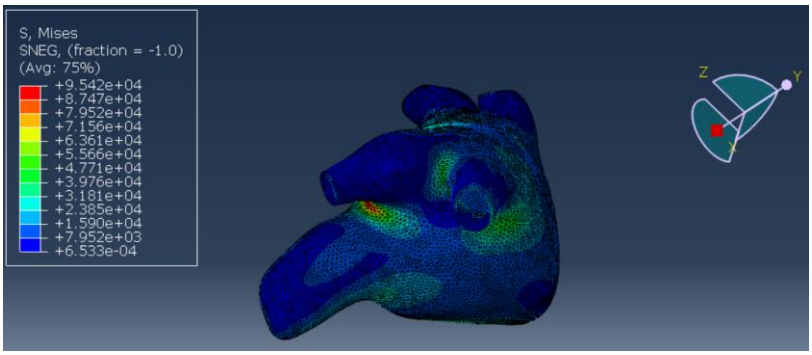

Figure 5.20: von Mises stress with AFIB left atrial pressure loading condition of 7.5 mmHg Image taken from Peak Pressure of Second Cardiac Cycle

CHAPTER 6: DISCUSSION AND CONCLUSION

In this study, the relationship between the ostial diameter of the left atrial appendage as well as the stresses and strains that the left atrium and appendage undergo in a patient-specific geometry were investigated. Simulations were run at 5 mmHg, 7.5 mmHg, 10 mmHg, 15 mmHg, and 20 mmHg in order to get an idea of the types of deformation that would be present. The simulations were performed using ABAQUS software and several different methods for obtaining material methods were investigated, with data from biaxial stretching of human tissue chosen as the final material model. Simulations were run primarily with a healthy cardiac cycle pressure but one case of atrial fibrillation pressure curve was tested without major differences between the two. Maximum in plane stress and corresponding ostial diameter for each of the simulation conditions are summarized in Table 6-1.

Table 6-1: Ostial Size and Stress of Patient-Specific Model at 0, 5, 10, 15, 20 and 7.5 mmHg

Average LAP (mmHg)	Ostial Size: Short Axis (cm)	Ostial Size: Long Axis (cm)	Max in-plane Stress (Pa)
0	1.347	2.927	-
5	1.578	3.021	5.674×10^4
10	1.653	3.090	1.252×10^5
15	1.670	3.162	1.991×10^5
20	1.749	3.219	2.556×10^5
.			
7.5	1.644	3.063	1.064×10^5 (Mises)
7.5 AFIB	1.626	3.054	9.542×10^4 (Mises)

Some trends that can be noted from the simulation results make sense from both a theoretical as well as physiological standpoint. Under physiological loading conditions, ostial diameter increases with increasing left atrial pressure. An interesting result is that deformation is much more prominent along the short axis of the opening when compared with the long axis, making the deformed shape of the LAA ostial diameter more circular

when a load is applied. At peak left atrial pressure during the second cycle of loading, maximum in plane stress is 56 kPa for 5 mmHg average load, and this increases up to 256 kPa for 20 mmHg average loading curve. While left atrial pressures of 20 mmHg are on the extreme end of the spectrum, these results suggest that sudden changes in left atrial pressure can have drastic effects on the stresses and strains experienced by the cardiac tissue. For patients with mechanical occlusion devices, especially those with atrial flutter or fibrillation, changes in left atrial pressure outside of what is normally expected could result in unforeseen deformation of the tissue, which may explain cases in which occlusion devices dislodge from their attachment site. Furthermore, peak stresses occur along the top and bottom of the long axis of the appendage rim and also around the pulmonary veins, rather than along the short axis of the opening and these stresses correspond to the high pressure points of the cardiac cycle, during atrial systole, and also during full filling of the atrium.

While the LAA varies in shape and size based on the individual, our results indicate that typical left atrial pressures tends to deform the ostial opening to the appendage in such a way that it becomes more circular in shape. Uneven spread of stress in the tissue also supports this conclusion, with higher stresses along the shorter axis of the ostial opening, when looked at as an ellipse. For patients with mechanical occlusion devices, these asymmetries in stress and strain may fatigue the material of the occlusion device asymmetrically, leading to uneven wear and tear, which may weaken the structural integrity of the device. For this patient specific study, the length of the short axis of the ostial diameter opening experienced an increase in size of 17.1% at loading of 5 mmHg up

to an increase in size of 29.9% at a loading of 20 mmHg. However, the long axis opening only experienced increases of 3.2% at 5 mmHg to up to 9.9% at 20 mmHg. This again highlights the asymmetrical deformation pattern of this particular patient-specific model that is likely due to the asymmetric, elliptical nature of the opening to the atrial appendage.

As for the comparison between loading with a healthy pressure curve versus loading with a pressure curve more characteristic of a patient with atrial fibrillation, the results indicate that there is not much difference. For the atrial fibrillation pressure loading curve that was used, both the ostial size as well as the von Mises stress were negligibly lower than the simulation results for the healthy pressure loading curve. This makes sense from a theoretical standpoint because while patients with atrial fibrillation tend to have a more erratic or fluttered cardiac cycle, the peak stresses experienced are not drastically different. From a purely biomechanical standpoint with considerations of passive tissue mechanics, one would not expect to see a large difference between the two test conditions. For live cardiac tissue, the unsteady cardiac cycle of patients with atrial fibrillation may further complicate and confound with the left atrial appendage from an excitation-contraction standpoint, but this angle still needs further exploration.

To summarize, several different methods for obtaining the material property inputs into a patient-specific finite element model were explored. Originally, biaxial stretching and DIC data collected from fresh ovine tissue samples were processed into stress-strain data inputs for the model, but differences between the species were drastic enough that the model was unrealistic. After obtaining raw data from biaxial stretching of human left atrium and left atrial appendage tissues, the data was fit to a 4-parameter Fung-type

exponential model successfully and served as inputs for the patient-specific model. The 3-D geometry of the model itself was collated from many slices of computed tomographic angiography images and meshed using Hypermesh. This model was then input into ABAQUS with triangular shell elements and the material properties extracted from the human biaxial stretch were used to perform simulations at 5, 7.5, 10, 15, and 20 mmHg left atrial pressure loading curves. Looking at the deformations at the ostial opening to the left atrial appendage along with the maximum in plane-stresses experienced by the models, our results indicate that deformation of the opening is asymmetric due to the elliptical shape of the appendage, and this finding may translate to other patients. In the future, with widespread access to medical imaging, performing simpler finite element simulations on patient-specific data may become a viable strategy for improving patient health outcomes, especially when it comes to the use of mechanical occlusion devices targeting patients with atrial fibrillation. There are also some ways to improve the modelling framework of this study. For the material model used, using DIC to quantify the 3D stress-strain behavior would allow use of a more accurate Fung model with more independent material parameters. Such a set-up could even be used to virtually implant a mechanical occlusion device and measure the impact directly, experimentally. Of course, one limitation of this study is its patient-specific nature, so increasing the number of samples would be beneficial. Other improvements could be made by having a distinct material model for the pulmonary veins, atrium, and appendage or by simulating the effects of the surrounding pericardium.

REFERENCES

1. Veinot J. P., et al. Anatomy of the Normal Left Atrial Appendage. Circulation 96: 3112-3115, 1997.
2. Contractor T., Khasnis A. Left Atrial Appendage Closure in Atrial Fibrillation: A World without Anticoagulation? Cardiology Research and Practice, 2011.
3. Healey J. S., et al. Left Atrial Appendage Occlusion Study (LAAOS): Results of a randomized controlled pilot study of left atrial appendage occlusion during coronary bypass surgery in patients at risk for stroke. American Heart Journal 150: 288-293, 2005.
4. Al-Saady N. M., et al. Left atrial appendage: structure, function, and role in thromboembolism. Heart 82: 547-555, 1999.
5. Beigel R., et al. The Left Atrial Appendage: Anatomy, Function, and Noninvasive Evaluation. JACC Cardiovascular Imaging 7, 2014.
6. Ernst G., et al. Morphology of the left atrial appendage. The Anatomical Record 242: 553-561, 1995.
7. Regazzoli D., et al. Left Atrial Appendage: Physiology, Pathology, and Role as a Therapeutic Target. Biomed Research International, 2015.
8. Stoddar M. F., et al. Left atrial appendage thrombus is not uncommon in patients with acute atrial fibrillation and a recent embolic event: a transesophageal echocardiographic study. Journal of the American College of Cardiology 25: 452-459, 1995.
9. Lang R. M., et al. Recommendations for chamber quantification. Journal of American Society of Echocardiography 12: 1440-1463, 2005.
10. Abe H., et al. Stress-strain relation of cardiac muscle determined from ventricular pressure-time relationships during isovolumic contractions. Journal of Biomechanics 14: 357-360, 1981.

11. Reddy V. Y., et al. Percutaneous left atrial appendage closure vs warfarin for atrial fibrillation: a randomized clinical trial. JAMA 312(19): 1988–1998, 2014.
12. U.S. Patent No. US8767049. (n.d.). Washington, DC: U.S. Patent and Trademark Office, 2016.
13. Brilla, C., Jacob, R., Kissling, G. Determination of left ventricular diastolic wall stress and elasticity in situ. A methodological investigation*). Cardiac Adaptation to Hemodynamic Overload, Training and Stress: 354-363, 1983.
14. Gao, B. Z., Pandya, S., Arana, C., Hwang, N. H. Bioprosthetic Heart Valve Leaflet Deformation Monitored by Double-Pulse Stereo Photogrammetry. Annals of Biomedical Engineering 30(1): 11-18, 2002.
15. Putter, S. D., Wolters, B., Rutten, M., Breeuwer, M., Gerritsen, F., Vosse, F. V. Patient-specific initial wall stress in abdominal aortic aneurysms with a backward incremental method. Journal of Biomechanics 40(5): 1081-1090, 2007.
16. Hasan, A., Ragaert, K., Swieszkowski, W., Selimović, Š, Paul, A., Camci-Unal, G., Mofrad M.R., Khademhosseini, A. Biomechanical properties of native and tissue engineered heart valve constructs. Journal of Biomechanics 47(9): 1949-1963, 2014.
17. Hokka, M., Mirow, N., Nagel, H., Irqsusi, M., Vogt, S., & Kuokkala, V. In-vivo deformation measurements of the human heart by 3D Digital Image Correlation. Journal of Biomechanics 48(10): 2217-2220, 2015.
18. Holzapfel, G. A., & Ogden, R. W. Constitutive modelling of passive myocardium: A structurally based framework for material characterization. Philosophical Transactions of the Royal Society A: Mathematical, Physical and Engineering Sciences 367(1902): 3445-3475, 2009.
19. Bellini A., et al. Mechanical Behavior of the Human Atria. Annals of Biomedical Engineering 41: 1478-90, 2013.
20. Javani S., Gordon M., Azadani A. N. Biomechanical Properties and Microstructure of Heart Chambers: A Paired Comparison Study in an Ovine Model. Annals of Biomedical Engineering 44(11): 3266-3283, 2016

21. Krishnamurthy A., Villongco C. T., Chuang J., Frank L. R., Nigam V., Belezzuoli E., et al. Patient-specific models of cardiac biomechanics. Journal of Computational Physics 244: 4-21, 2013.
22. Krishnamurthy A., Villongco C., Beck A., Omens J., Mcculloch A. Left Ventricular Diastolic and Systolic Material Property Estimation from Image Data. Lecture Notes in Computer Science Statistical Atlases and Computational Models of the Heart - Imaging and Modelling Challenges: 63-73, 2015
23. Krishnamurthy G., Itoh A., Bothe W., Swanson J. C., et al. Stress–strain behavior of mitral valve leaflets in the beating ovine heart. Journal of Biomechanics 42(12): 1909-1916, 2009.
24. Lee M., Holdsworth D., Fenster A. Dynamic 3D computed tomography: Non-invasive method for determination of the aortic dynamic elastic modulus. Proceedings of the 22nd Annual International Conference of the IEEE Engineering in Medicine and Biology Society: (Cat. No.00CH37143), 2000.
25. Nakamura T., Abe H., Arai S., Kimura T., Kushibiki H., Motomiya, M., et al. The stress-strain relationship of the diastolic cardiac muscle and left ventricular compliance in the pressure-overload canine heart. Japanese Circulation Journal 46(1): 76-83, 1982.
26. Riveros F., Chandra S., Finol E. A., Gasser, T. C., Rodriguez J. F. A Pull-Back Algorithm to Determine the Unloaded Vascular Geometry in Anisotropic Hyperelastic AAA Passive Mechanics. Annals of Biomedical Engineering 41(4): 694-708, 2012.
27. Rizzuto E., Carosio S., Prete Z. D. Characterization of a Digital Image Correlation System for Dynamic Strain Measurements of Small Biological Tissues. Experimental Techniques: 2014.
28. Stefano L. D., Matsubara L., Matsubara B. Myocardial contractility of the isovolumetrically beating isolated rat heart. Brazilian Journal of Medical and Biological Research 37(10): 1563-1569, 2004.

29. Zhao F., Chen J., Blagg A., Berretta R., Margulies K. An integrated method to determine the stress-strain relationship of beating heart. 2003 IEEE 29th Annual Proceedings of Bioengineering Conference: n.d.
30. Toma M., Bloodworth C. H., Einstein D. R., Pierce E. L., Cochran R. P., Yoganathan A. P., Kunzelman K. S. High-resolution subject-specific mitral valve imaging and modeling: experimental and computational methods. Biomechanics and Modeling in Mechanobiology Biomech Model Mechanobiol: 2016.
31. Pierce E. L., Bloodworth C. H., Naran A., Easley T. F., Jensen M. O., Yoganathan A. P. Novel Method to Track Soft Tissue Deformation by Micro-Computed Tomography: Application to the Mitral Valve. Annals of Biomedical Engineering Ann Biomed Eng 44: 2273–2281. 2015.
32. Krishnamurthy A., Villongco C., Beck A., Omens J., Mcculloch A. Left Ventricular Diastolic and Systolic Material Property Estimation from Image Data. Lecture Notes in Computer Science Statistical Atlases and Computational Models of the Heart - Imaging and Modelling Challenges: 63–73, 2015.
33. Krishnamurthy A., Villongco C. T., Chuang J., Frank L. R., Nigam V., Belezzuoli E., Stark P., Krummen D. E., Narayan S., Omens J. H., McCulloch A. D., Kerckhoffs R. C. Patient-specific models of cardiac biomechanics. Journal of Computational Physics 244: 4–21, 2013.
34. Krishnamurthy G., Itoh A., Bothe W., Swanson J. C., Kuhl E., Karlsson M., Miller D. C., Ingels N. B. Stress–strain behavior of mitral valve leaflets in the beating ovine heart. Journal of Biomechanics 42: 1909–1916, 2009.
35. Humphrey J. Cardiovascular Solid Mechanics: Cells, Tissues, and Organs. Springer, 2010.
36. Lindley E., Whisenant B. Percutaneous left atrial appendage closure: a review of the WATCHMAN clinical trial experience. Device Evaluations - Interventional Cardiology 7: 2015.

37. Robertson D. and D. Cook. Unrealistic statistics: How average constitutive coefficients canproduce non-physical results. J Mech Behav Biomed Mater 40: 234-239, 2014.
38. Langdon S., Chernecky R., Pereira C., Abdulla D., Lee J. Biaxial mechanical/structural effects of equibiaxial strain during crosslinking of bovine pericardial xenograft materials. Biomaterials 20: 137-53, 1999.
39. Matsumoto, Takeo, et al. Biaxial Tensile Properties of Thoracic Aortic Aneurysm Tissues. Journal of Biomechanical Science and Engineering 4:518-529, 2009.
40. Y.C. Fung, K. Fronek, P. Patitucci. Pseudoelasticity of arteries and the choice of its mathematical expression. Am. J. Physiol. 237: H620-H631, 1979.

Appendix

Selected Material Property Inputs into ABAQUS: Biaxial Hyperelastic Input Poisson = 0.449, Rows 1-100 and 401-500.

Row: 1-100 Nominal Stress (Pa)	*Row: 1-100 Nominal Strain*	*Row: 401-500 Nominal Stress (Pa)*	*Row: 401-500 Nominal Strain*
0	0	22693.7	0.183555
10.4888	0.000501	22921.3	0.183978
20.9991	0.001002	23151.4	0.184401
31.5315	0.001502	23384.1	0.184824
42.0865	0.002002	23619.4	0.185247
52.6646	0.002502	23857.3	0.185669
63.2665	0.003002	24097.8	0.186092
73.8925	0.003501	24341	0.186514
84.5433	0.004	24587	0.186936
95.2195	0.004499	24835.6	0.187358
105.921	0.004998	25087.1	0.18778
116.65	0.005496	25341.3	0.188202
127.405	0.005994	25598.4	0.188623
138.188	0.006492	25858.4	0.189045
148.999	0.00699	26121.3	0.189466
159.839	0.007487	26387.1	0.189887
170.708	0.007984	26655.9	0.190308
181.607	0.008481	26927.8	0.190729
192.536	0.008978	27202.7	0.19115
203.496	0.009474	27480.7	0.19157
214.488	0.00997	27761.9	0.191991
225.511	0.010466	28046.2	0.192411
236.568	0.010962	28333.8	0.192831
247.657	0.011457	28624.6	0.193251
258.781	0.011953	28918.7	0.193671
269.939	0.012448	29216.1	0.19409
281.132	0.012942	29516.9	0.19451
292.361	0.013437	29821.2	0.194929

303.626	0.013931	30128.9	0.195348
314.928	0.014425	30440.1	0.195767
326.267	0.014919	30754.9	0.196186
337.645	0.015412	31073.2	0.196605
349.061	0.015906	31395.2	0.197024
360.517	0.016399	31720.9	0.197442
372.012	0.016891	32050.4	0.19786
383.549	0.017384	32383.6	0.198279
395.126	0.017876	32720.6	0.198697
406.745	0.018368	33061.5	0.199115
418.407	0.01886	33406.4	0.199532
430.112	0.019352	33755.2	0.19995
441.861	0.019843	34108	0.200367
453.654	0.020334	34465	0.200785
465.493	0.020825	34826	0.201202
477.377	0.021316	35191.2	0.201619
489.307	0.021806	35560.7	0.202036
501.285	0.022297	35934.4	0.202452
513.311	0.022787	36312.5	0.202869
525.385	0.023276	36695	0.203285
537.508	0.023766	37081.9	0.203702
549.681	0.024255	37473.4	0.204118
561.904	0.024744	37869.4	0.204534
574.179	0.025233	38270	0.20495
586.506	0.025721	38675.3	0.205365
598.885	0.02621	39085.4	0.205781
611.318	0.026698	39500.3	0.206196
623.805	0.027186	39920	0.206612
636.347	0.027673	40344.6	0.207027
648.944	0.028161	40774.3	0.207442
661.598	0.028648	41209	0.207857
674.308	0.029135	41648.8	0.208271
687.076	0.029621	42093.8	0.208686
699.903	0.030108	42544.1	0.2091
712.789	0.030594	42999.7	0.209515
725.735	0.03108	43460.6	0.209929

738.742	0.031566	43927.1	0.210343
751.81	0.032052	44399	0.210757
764.941	0.032537	44876.6	0.21117
778.135	0.033022	45359.8	0.211584
791.393	0.033507	45848.8	0.211997
804.715	0.033991	46343.6	0.212411
818.103	0.034476	46844.3	0.212824
831.558	0.03496	47351	0.213237
845.079	0.035444	47863.7	0.21365
858.669	0.035928	48382.6	0.214063
872.327	0.036411	48907.6	0.214475
886.055	0.036895	49439	0.214888
899.853	0.037378	49976.7	0.2153
913.723	0.03786	50520.9	0.215712
927.664	0.038343	51071.6	0.216124
941.679	0.038826	51629	0.216536
955.768	0.039308	52193	0.216948
969.931	0.03979	52763.9	0.217359
984.171	0.040271	53341.6	0.217771
998.486	0.040753	53926.4	0.218182
1012.88	0.041234	54518.2	0.218593
1027.35	0.041715	55117.2	0.219004
1041.9	0.042196	55723.4	0.219415
1056.53	0.042677	56337	0.219826
1071.24	0.043157	56958	0.220237
1086.04	0.043637	57586.6	0.220647
1100.92	0.044117	58222.9	0.221058
1115.88	0.044597	58866.9	0.221468
1130.92	0.045076	59518.7	0.221878
1146.05	0.045556	60178.5	0.222288
1161.27	0.046035	60846.4	0.222698
1176.58	0.046513	61522.5	0.223108
1191.97	0.046992	62206.8	0.223517
1207.46	0.047471	62899.5	0.223926
1223.03	0.047949	63600.8	0.224336